Chapter 8
Weak Focusing Synchrotron

Abstract This chapter introduces the weak focusing synchrotron, and the theoretical material needed for the simulation exercises. It begins with a brief reminder of the historical context, and continues with the beam optics and acceleration techniques that the weak focusing synchrotron principle and methods lean on, relying on basic charged particle optics and acceleration concepts introduced in the previous chapters. It further addresses the following aspects:
- fixed closed orbit,
- periodic structure,
- periodic motion stability,
- optical functions,
- synchrotron motion,
- depolarizing resonances.

The simulation of a weak focusing synchrotron lattice only requires two optical elements: DIPOLE or BEND to simulate combined function dipoles, and DRIFT to simulate straight sections. A third element, CAVITE, is required for acceleration. Computation of synchrotron radiation (SR) Poynting and spectral brightness uses `zpop`. Particle monitoring requires keywords introduced in the previous chapters, including FAISCEAU, FAISTORE, PICKUPS, and some others. Spin motion computation and monitoring resort to SPNTRK, SPNPRT and FAISTORE. Optics matching and optimization use FIT[2]. INCLUDE is used, mostly here in order to shorten the input data files. SYSTEM is used to, mostly, resort to gnuplot so as to end simulations with some specific graphs (orbits, fields, or else) obtained by reading data from output files such as zgoubi.fai (resulting from the use of FAISTORE), zgoubi.plt (resulting from IL=2), or other zgoubi.*.out files resulting from a PRINT command.

DRAFT

4769 ## Notations used in the Text

B; $\mathbf{B}$; $B_{\mathrm{x,y,s}}$	field; field vector; its components in the moving frame
$B\rho = p/q$; $B\rho_0$	particle rigidity; reference rigidity
C; C_0	orbit length, $C = 2\pi R + \left[\begin{smallmatrix}\text{straight}\\ \text{sections}\end{smallmatrix}\right.$; reference, $C_0 = C(p = p_0)$
$\mathbf{E}$; E_σ, E_π	SR electric field impulse; its parallel and normal components
E; E_s	particle energy, $E = \gamma m_0 c^2$; synchronous energy
EFB	Effective Field Boundary
f_{rev}, $f_{\mathrm{rf}} = h\, f_{\mathrm{rev}}$	revolution and RF voltage frequencies
G	gyromagnetic anomaly, $G = 1.792847$ for proton
h	RF harmonic number, $h = f_{\mathrm{rf}}/f_{\mathrm{rev}}$
m; m_0; M	particle mass; rest mass; mass in units of MeV/c^2
$n = -\frac{\rho}{B}\frac{\partial B}{\partial x}$	focusing index
$\mathbf{n}_0$	stable spin precession direction
$\mathbf{p}$; p; p_0	momentum vector; its modulus; reference
$\mathbf{P} = \mathbf{E} \times \mathbf{B}$	SR Poynting vector
P_i, P_f	beam polarization, initial, final
q	particle charge
R	average orbit radius, $R = C/2\pi$
s	path variable
v	particle velocity
4770 $V(t)$; $\hat{V}$	oscillating voltage; its peak value
x, x', y, y'	horizontal and vertical coordinates in the moving frame
α	momentum compaction; or trajectory deviation; or depolarizing resonance crossing speed
$\beta = v/c$; β_0; β_{s}	normalized particle velocity; reference; synchronous
β_{u}	betatron functions ($u:\ x, y$)
$\gamma = E/m_0c^2$	Lorentz relativistic factor
δp, Δp	momentum offset
ϵ_c	critical energy of SR, $\epsilon_c = \hbar\omega_c = hc/\lambda_c$
ε	wedge angle
ε_u	Courant-Snyder invariant; or beam emittance ($u:\ x, y, l$)
ϵ_R	strength of a depolarizing resonance
μ_{u}	betatron phase advance per period, $\mu_{\mathrm{u}} = \int_{\mathrm{period}} \frac{ds}{\beta_{\mathrm{u}}(s)}$ ($u:\ x, y$)
ν_{u}	wave numbers, horizontal, vertical, synchrotron ($u:\ x, y, l$)
ρ; ρ_0	curvature radius; reference
σ	beam matrix
ϕ; ϕ_{s}	particle phase at voltage gap; synchronous phase
φ	spin angle to the vertical axis
ω	angular frequency
ω_c	critical angular frequency of SR, $\omega_c = 3\gamma^3 c/2\rho$

DRAFT

8.1 Introduction

The synchrotron is an outcome of the mid-1940s phase focusing resonant acceleration concept [1, 2]. Phase focusing, or synchronous, acceleration with slow variation of the magnetic field to maintain the beam on a constant orbit and constant RF phase was demonstrated with the acceleration of electrons from 4 to 8 MeV, in an existing betatron, using fixed RF, in 1946 [3]. This proof-of-principle was closely followed by the construction and operation, at GEC, of a 70 MeV synchrotron (weak focusing... no other choice at the time). The latter happened to be the opportunity for the first observation of visible SR, a serendipity resulting from the fact that the vacuum chamber was made of glass [4]. Observations included color of the radiation changing from blue to yellow when energy was decreased to 40 MeV[1] [5] - more in the Poynting simulation exercise 8.3. Measurements of properties of the radiation were undertaken at the time, whereas SR acquired a status of a beam monitoring tool, that was the beginning of a long story, still underway...

Transverse beam confinement in the weak focusing synchrotron version of the synchrotron, over the thousands of turns needed for acceleration to top energy, was based on the technique known at the time, inherited from cyclotron and betatron: weak focusing,

Phase focusing states that stability of longitudinal motion (longitudinal focusing), is obtained if the particles in a bunch arrive at the accelerating gap in the vicinity of a proper phase of the oscillating voltage, the synchronous phase, such that the bunch stays together during acceleration. Synchrotrons operate in general in a non-isochronous regime: the revolution period changes with energy. As a consequence the RF, $f_{\mathrm{rf}} = h f_{\mathrm{rev}}$, has to change continuously from injection to top energy in order to maintain an accelerated bunch on the synchronous phase. The reference orbit in a synchrotron is maintained at constant radius by ramping the guiding field in the main dipoles in synchronism with the acceleration, as in the betatron [6].

The synchrotron concept increased the energy reach of particle accelerators at the time. It led to the construction of a series of proton rings with increasing energy [8]: 1 GeV at Birmingham (1953), 3.3 GeV at the Cosmotron (Brookhaven National Laboratory, 1953-1969), 6.2 GeV at the Bevatron (Berkeley, 1954-1993), 10 GeV at the Synchro-Phasotron (JINR, Dubna, 1957-2003), and a few others in the late 1950s. Weak focusing magnets are quite bulky, creating a practical limit to further increase in energy[2]. This issue was overcome with the strong focusing method, devised in the early 1950s (Chap. 9). The general layout of these first weak focusing synchrotrons included straight sections (often 4, Fig. 8.1), to allow for the insertion of injection and extraction systems, accelerating cavities, orbit correction and beam monitoring equipment.

DRAFT

---

[1] At 70 MeV with a bending radius of say 0.5 m, the critical wavelength $\lambda_c = 4\pi\rho/3\gamma^3$ (Sect. 5.2.3) falls in the visible range.

[2] The story has it that it was possible to ride a bicycle in the vacuum chamber of Dubna's Synchro-Phasotron.

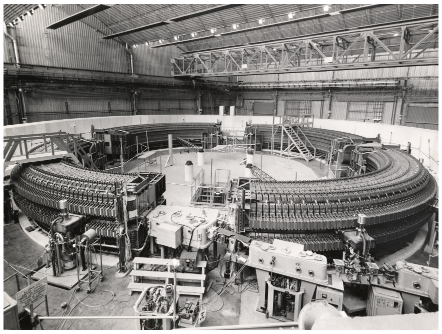

Fig. 8.1 SATURNE 1 at Saclay [7], a 3 GeV, 4-period, 68.9 m circumference, weak focusing synchrotron, constructed in 1956-58. The injection line is seen in the foreground. Injection is from a 3.6 MeV Van de Graaff (not visible)

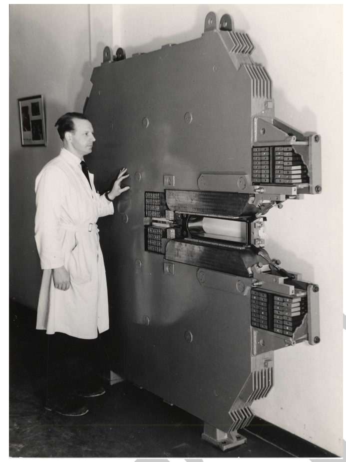

Fig. 8.2 A slice of the SATURNE 1 dipole [7]. The slight gap tapering, increasing outward, determines the weak index condition $0 < n < 1$

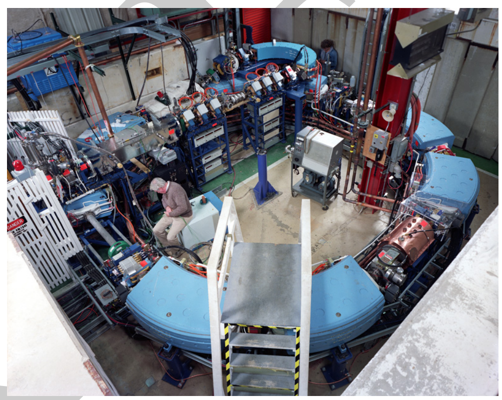

Fig. 8.3 Loma Linda University medical synchrotron [9], during commissioning in 1989 at the Fermilab National Accelerator Laboratory where it was designed

The weak focusing synchrotron was used in fixed-target nuclear and particle physics, material science, medicine, industry, etc. Remarkably, it was a landmark (if not the starting point[3]) of the history of collider rings, the AdA *Anello di Accumulazione*, which demonstrated long term beam storage (and the Touschek effect), and produced the first e+e- collisions in the early 1960s, was a weak focusing synchrotron, a 250 MeV ring based on a $n = 0.55$ gradient dipole [14].

[3] The third electron model built by the MURA group, a 50 MeV fixed field alternating gradient (FFAG) ring, started in 1961, was operated in collider mode with two counter-rotating electron beams [12, 13].

DRAFT

Fig. 8.4 The ZGS at Argonne during construction [15]. A 12 GeV, 8-dipole, 4-period, 172 m circumference, wedge focusing synchrotron. The two persons inside and outside the ring, in the background, give an idea of the size of the magnets

Polarized beams

Synchrotrons allowed the acceleration of polarized beams to high energy[4]. The possibility was considered from the early times at Argonne ZGS (Zero-Gradient Synchrotron), a 12 GeV weak focusing synchrotron operated over 1964-1979 [16] (Fig. 8.4). ZGS accelerated polarized proton beams to 17.5 GeV/c with *appreciable polarization* [17]. Polarization preservation techniques included harmonic orbit correction and fast betatron tune jumps at the strongest depolarizing resonances [18] (*cf.* Sect. 8.2.4, Fig. 8.19). Experiments were performed to assess the possibility of polarization transmission in strong focusing synchrotrons, and potential polarization lifetime in colliders [19]. Acceleration of polarized deuteron was achieved in the late 1970s [20].

The weak focusing synchrotron is still topical today, due for a large part to its relative simplicity, with low energy beam application where relatively low current is not a concern, such as in the hadrontherapy (Fig. 8.3) [10, 11]. It only requires a single type of a simple weak gradient dipole, a single power supply, a single accelerating gap. It has an advantage of beam manipulation flexibility, when needed, compared to (synchro-)cyclotrons.

8.2 Basic Concepts and Formulæ

The synchrotron is based on two key principles. First, a slowly varying magnetic field maintains a constant orbit during acceleration,

$$B(t)\,\rho = p(t)/q, \quad \rho = constant, \tag{8.1}$$

[4] Polarized proton and deuteron beams had been accelerated in electrostatic columns (Sect. 2.1), and soon after in cyclotrons, when polarized beam sources were made available.

DRAFT

with $p(t)$ the particle momentum and ρ the bending radius in the dipoles. Second, longitudinal phase stability enables synchronous acceleration. In a regime where velocity change with energy cannot be ignored (non-ultrarelativistic particles), the latter requires a modulation of the accelerating voltage frequency to satisfy

$$f_{\mathrm{rf}}(t) = h f_{\mathrm{rev}}(t) \qquad \text{with h an integer} \tag{8.2}$$

Synchronism between accelerating voltage oscillations and particle revolution keeps the bunch on a synchronous phase. Synchronous acceleration is technologically simpler in the case of electrons above a few MeV, because frequency modulation is unnecessary. For instance, from $v/c = 0.9987$ at 10 MeV to $v/c \to 1$ the relative change in revolution frequency amounts to $\delta f_{\mathrm{rev}}/f_{\mathrm{rev}} = \delta\beta/\beta < 0.0013$.

Varying field and RF on the one hand, fixed orbit in addition, are major evolutions compared to cyclotron, where instead, field and RF are fixed, and the accelerated orbit spirals out. A fixed orbit reduces the radial extent of individual guiding magnets, allowing a structure comprised of a circular string of dipoles. A synchrocyclotron instead uses a single, massive dipole (the volume of iron increases more than quadratically with bunch rigidity) with a wide radial extent allowing for a span of the field integral over $\oint B_{\mathrm{injection}}\, dl = \frac{2\pi p_{\mathrm{min}}}{q} - \oint B_{\mathrm{extraction}}\, dl \frac{2\pi p_{\mathrm{max}}}{q}$,

Either a weak index ($-1 < k < 0$, Sect. 3.2.2) and/or wedge focusing (*cf.* Sect. 14.4.1) are used in weak focusing synchrotrons. Transverse stability was based solely on the latter at Argonne ZGS. Weak focusing in the ZGS resulted in weak depolarizing resonances, an advantage in that matter [19].

The synchrotron is a pulsed accelerator due to the necessary ramping of the field in order to maintain a constant orbit. The acceleration is cycled, from injection to top energy, repeatedly. The cycling repetition rate depends on the type of power supply. If the ramping uses a constant electromotive force, then

$$B(t) \propto (1 - e^{-\frac{t}{\tau}}) = 1 - \left[1 - \left(\frac{t}{\tau}\right) + \left(\frac{t}{\tau}\right)^2 - \ldots\right] \approx \frac{t}{\tau} \tag{8.3}$$

essentially linear. $\dot{B} = dB/dt$ does not exceed a few Tesla/second, the repetition rate of the acceleration cycle if of the order of a Hertz. If instead the magnet winding is part of a resonant circuit then the field oscillates from an injection threshold to a maximum value, $B(t) : B_0 \to B_0 + \hat{B}$, as in the betatron. In this case the repetition rate can be up to a few tens of Hertz. In both cases anyway B imposes its law and the other quantities, RF frequency in particular, follow.

For comparison: in a synchrocyclotron the field is constant, thus acceleration can be cycled as fast as the swing of the voltage frequency allows (hundreds of Hz are common practice). A conservative 10 kVolts per turn requires of the order of 10,000 turns for a proton to reach 100 MeV, with velocity $0.046 < v/c < 0.43$ from 1 to 100 MeV. Take $v \approx c$ for simplicity, and a circumference of a few meters, the acceleration thus takes $\approx 10^4 \times C/c$ ≈millisecond, potentially allowing a repetition rate in the kHz range, more than an order of magnitude beyond the reach of a rapid-cycling pulsed synchrotron.

DRAFT

8.2.1 Periodic Stability

This section introduces various ingredients concerning transverse focusing and the conditions for periodic stability. It builds on material introduced in Chap. 3, Classical Cyclotron.

8.2.1.1 Closed orbit

The closed orbit is fixed, as in the betatron, and maintained during acceleration by ensuring that the relationship of Eq. 8.1 is satisfied. In a perfect ring, the closed orbit is along an arc in the bending magnets and straight along the drifts, Fig. 8.5. Particle motion is defined in the Serret-Frénet frame (O;s,x,y), Fig. 3.8.

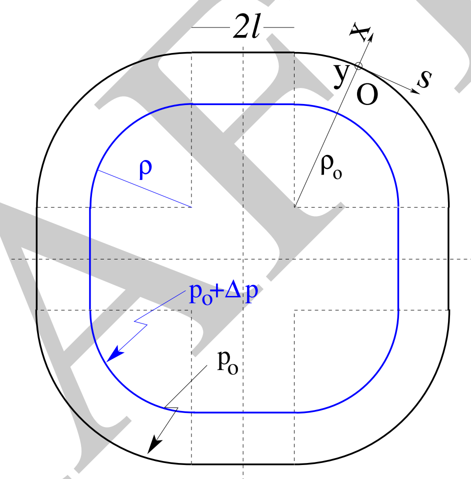

Fig. 8.5 A 4-fold symmetric structure with four drift spaces of length $2l$. Orbit length on reference momentum p_0 is $C = 2\pi\rho_0 + 8l$. (O;s,x,y) is the moving frame, along the reference orbit. The orbit for momentum $p = p_0 + \Delta p$ ($\Delta p < 0$, here) is at constant distance $\Delta x = D_x \frac{\Delta p}{p_0}$ from the reference orbit

8.2.1.2 Transverse Focusing

Radial motion stability around a reference closed orbit in an axially symmetric dipole field requires a field index (Sect. 3.2.2),

$$n = -\frac{\rho_0}{B_0}\frac{\partial B_y}{\partial x}\bigg|_{x=0,\ y=0} \tag{8.4}$$

This quantity, evaluated on the reference arc in the dipoles, satisfies the weak focusing condition (Eq. 3.12 with $n = -k$)

$$0 < n < 1 \tag{8.5}$$

DRAFT

This condition can be obtained with a tapered gap (as in SATURNE 1 dipole, Fig. 8.2) resulting in both radial and axial focusing (Figs. 8.6, 8.7). Note the sign convention here, opposite to that used for the cyclotron (Eq. 3.11). This condition holds regardless of the presence or not of drifts. Adding drifts brings to defining two radii, namely,

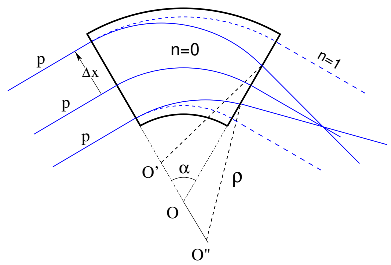

Fig. 8.6 Geometrical focusing: in a sector dipole with focusing index $n = 0$, parallel incoming rays of equal momenta experience the same curvature radius ρ, so their trajectories converge as outer trajectories have a longer path in the field. An index value n=1 cancels that effect: parallel incoming rays exit parallel

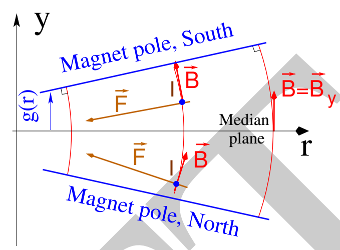

Fig. 8.7 Axial motion stability requires proper shaping of field lines: B_y has to decrease with radius. The Laplace force pulls a positive charge (located at I) with velocity pointing out of the page, toward the median plane. Increasing the field gradient (n closer to 1, gap opening up faster) increases the focusing

(i) the magnet curvature radius ρ_0,

(ii) an average radius $R = C/2\pi = \rho_0 + Nl/\pi$ (with C the length of the reference closed orbit, N the number of drifts and $2l$ their length) (Fig. 8.5) which can also be written

$$R = \rho_0(1+k), \qquad k = \frac{Nl}{\pi\rho_0} \tag{8.6}$$

Adding drift spaces decreases the average focusing around the ring.

Geometrical focusing

The limit $n \to 1$ of the transverse motion stability domain corresponds to a cancellation of the geometrical focusing (Fig. 8.6): in a constant field dipole (radial field index n=0) the longer (respectively shorter) path in the magnetic field for parallel trajectories entering the magnet at greater (respectively smaller) radius result in convergence. This effect is cancelled (*i.e.*, the bend angle is the same whatever the entrance radius) if the curvature center is made independent of the entrance radius: $OO' = 0$, $O''O = 0$. This occurs if trajectories at an outer (inner) radius experience a smaller (greater) field such as to satisfy $BL = B\rho\,\alpha = C^{st}$. Differentiating $B\rho = C^{st}$ gives $\frac{\Delta B}{B} + \frac{\Delta\rho}{\rho} = 0$, with $\Delta\rho = \Delta x$, so yielding $n = -\frac{\rho_0}{B_0}\frac{\Delta B}{\Delta x} = 1$. The focal distance associated with the curvature is (Eq. 3.13 with $R = \rho_0$) $f = \frac{\rho_0^2}{\mathcal{L}}$.

DRAFT

Wedge Focusing

Entrance and exit wedge angles may be used to ensure transverse focusing, Fig. 8.8: opening the magnetic sector increases the horizontal focusing (and decreases the vertical focusing); closing the magnetic sector has the reverse effect (*cf.* Sect. 14.4.1).

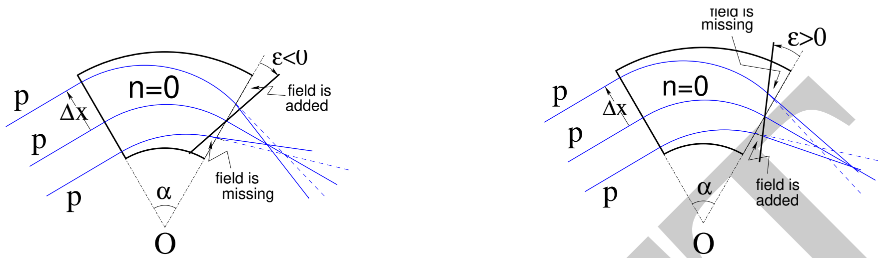

Fig. 8.8 Left: a focusing wedge ($\varepsilon < 0$); opening the sector increases horizontal focusing and decreases vertical focusing. Right: a defocusing wedge ($\varepsilon > 0$), closing the sector, has the reverse effect. This is the origin of the focusing in the ZGS zero-gradient dipoles

At the wedge the trajectory undergoes a deviation proportional to the distance to the optical axis, amounting to

$$\Delta x' = \frac{\tan\varepsilon}{\rho_0}\Delta x, \quad \Delta y' = -\frac{\tan(\varepsilon-\psi)}{\rho_0}\Delta y \tag{8.7}$$

The angle ψ is a correction for the fringe field extent (Eq. 14.21); the effect is of the first order on the vertical focusing, and second order horizontally.

Profiling the magnet gap in order to adjust the focal distance complicates the magnet; a parallel gap, $n = 0$, makes it simpler, for that reason edge focusing may be preferred. The method benefited the acceleration of polarized beams in the ZGS, as radial field components (which are responsible for depolarization), met at the EFBs of the eight main dipoles, where therefore weak [17]. Preserving beam polarization at high energy required tight control of the tunes, achieved at the 0.01 level by means of pole face winding added at the ends of the dipoles [21, 22].

Drawbacks of the weak focusing method include interdependence of radial and axial focusing, see *Working point* Section, below.

8.2.1.3 Betatron Motion

The first order differential equations of motion in the moving frame (Fig. 8.5) derive from the Lorentz equation

DRAFT

$$\frac{dm\mathbf{v}}{dt} = q\mathbf{v}\times\mathbf{B} \;\Rightarrow\; m\frac{d}{dt}\left\{\begin{array}{c}\frac{ds}{dt}\mathbf{s}\\ \frac{dx}{dt}\mathbf{x}\\ \frac{dy}{dt}\mathbf{y}\end{array}\right\} = q\left\{\begin{array}{c}\left(\frac{dx}{dt}B_y - \frac{dy}{dt}B_x\right)\mathbf{s}\\ -\frac{ds}{dt}B_y\mathbf{x}\\ \frac{ds}{dt}B_x\mathbf{y}\end{array}\right\} \tag{8.8}$$

Motion in a weak index dipole field is solved in Sect. 3.2.2, Classical Cyclotron chapter: in Eq. 3.7 substitute ρ to R, $n = -\frac{\rho_0}{B_0}\frac{\partial B_y}{\partial x}$ to $-k$ (Eq. 3.11), and evaluate on the reference orbit. Taylor expansions of the transverse field components in the moving frame lead to

$$\begin{aligned} B_y(\rho)|_{\mathrm{y=0}} &= B_0(1 - n\tfrac{x}{\rho_0}) + O(x^2)\\ B_x(0+y) &= -n\tfrac{B_0}{\rho_0}y + O(y^3) \end{aligned} \tag{8.9}$$

Assume transverse stability: $0 < n < 1$. In the approximation $ds \approx vdt$ (Eq. 3.14) Eqs. 8.8, 8.9 lead to the differential equations of motion

$$\frac{d^2x}{ds^2} + \frac{1-n}{\rho_0^2}x = 0, \quad \frac{d^2y}{ds^2} + \frac{n}{\rho_0^2}y = 0 \tag{8.10}$$

In an periodic structure comprised of gradient dipoles, wedges and drift spaces, the differential equation of motion takes the general form of Hill's equation, namely (with u standing for x or y),

$$\left\{\begin{array}{l}\dfrac{d^2u}{ds^2} + K_{\mathrm{u}}(s)u = 0\\ K_{\mathrm{u}}(s+S) = K_{\mathrm{u}}(s)\end{array}\right. \quad \text{with} \left\{\begin{array}{l}\text{in dipoles : }\left\{\begin{array}{l}K_x = \frac{1-n}{\rho_0^2}\\ K_y = \frac{n}{\rho_0^2}\end{array}\right.\\ \text{at a wedge at } s = s_0 : \; K_{\substack{x\\y}} = \frac{\pm\tan\varepsilon}{\rho_0}\delta(s-s_0)\\ \text{in drift spaces : } \frac{1}{\rho_0} = 0,\; K_x = K_y = 0\end{array}\right. \tag{8.11}$$

Here $K_{\mathrm{u}}(s)$ is periodic, $S = 2\pi R/N$ ($S = C/4$ for instance in a 4-period ring, Figs. 8.1, 8.5).

The solution of Eqs. 8.11 is not as straightforward as in the cyclotron where a constant K_{u} around the ring (Eq. 3.15) results in a sinusoidal motion (Eq. 3.17). A sinusoidal motion, with adding drifts, however remains a reasonable approximation, see below, *Weak focusing approximation*.

Floquet established [23] that the two independent solutions of Hill's second order differential equation with periodic coefficient have the form [24]

$$\left\{\begin{array}{l}u_1(s) = \sqrt{\beta_{\mathrm{u}}(s)}\,e^{\,i\int_0^s \frac{ds}{\beta_{\mathrm{u}}(s)}}\\ du_1(s)/ds = \dfrac{i-\alpha_{\mathrm{u}}(s)}{\beta_{\mathrm{u}}(s)}\,u_1(s)\end{array}\right. \quad \text{and} \quad \left\{\begin{array}{l}u_2(s) = u_1^*(s)\\ du_2(s)/ds = du_1^*(s)/ds\end{array}\right. \tag{8.12}$$

where $\beta_{\mathrm{u}}(s)$ and $\alpha_{\mathrm{u}}(s) = -\beta'_{\mathrm{u}}(s)/2$ are periodic functions, from what it results that

DRAFT

$$u_{\frac{1}{2}}(s+S) = u_{\frac{1}{2}}(s)\, e^{\pm i \int_{s_0}^{s} \frac{ds}{\beta_u(s)}} \tag{8.13}$$

where $\int_{s_0}^{s} \frac{ds}{\beta_u(s)}$ is the betatron phase advance at s, from the origin s_0. A real solution of Hill's equation is the linear combination $A\, u_1(s) + A^*\, u_2^*(s)$. With $A = \frac{1}{2}\sqrt{\varepsilon_u/\pi}\, e^{i\phi}$ following conventional notations, ϕ the phase of the motion at the origin $s = s_0$, the general solution of Eq. 8.11 is

$$\begin{cases} u(s) = \sqrt{\beta_u(s)\varepsilon_u/\pi}\, \cos\left(\int_{s_0}^{s} \frac{ds}{\beta_u} + \phi\right) \\ u'(s) = -\sqrt{\frac{\varepsilon_u/\pi}{\beta_u(s)}}\, \sin\left(\int_{s_0}^{s} \frac{ds}{\beta_u} + \phi\right) + \alpha_u(s)\, \cos\left(\int_{s_0}^{s} \frac{ds}{\beta_u} + \phi\right) \end{cases} \tag{8.14}$$

The Courant-Snyder invariant of the motion is

$$\frac{\varepsilon_u}{\pi} = \frac{1}{\beta_u(s)}\left[u^2 + (\alpha_u(s)u + \beta_u(s)u')^2\right] \tag{8.15}$$

At a given azimuth s of the periodic structure the observed turn-by-turn motion lies on that ellipse (Fig. 8.9). The form and orientation of the ellipse feature a weak dependence on the observation azimuth s, via the respective local values of $\alpha_u(s)$ (small at all s) and $\beta_u(s)$ (weakly modulated), and its area ε_u is an invariant. Equation 8.14 taken for $\alpha_u(s) = 0$ (an observation azimuth s where the ellipse is upright) shows that motion along the ellipse is clockwise. Note that in the coordinate

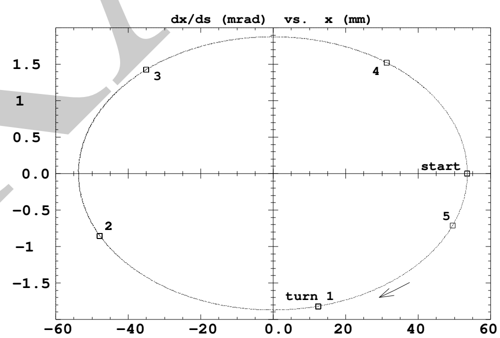

Fig. 8.9 A thousand passes in a ZGS 43 m cell, observed at the center of the long drift where $\alpha_x(s) = 0$, materialize the upright horizontal Courant-Snyder invariant. The first five passes are marked, motion goes clockwise with a cell phase advance of $0.21 \times 2\pi$. The aspect ratio of the ellipse only weakly depends on s, its area ($\varepsilon_x = 100\pi\,\mu$rad here) is an invariant of the motion

system $(u, (\alpha_u(s)u + \beta_u(s)u')$ the particle moves on a circle of radius ε_u/π.

The phase advance over a turn (from one position to the next on the ellipse, Fig. 8.9) in an N-periodic ring yields the wave number

$$\nu_u = \frac{1}{2\pi}\int_{s_0}^{s_0+NS} \frac{ds}{\beta_u(s)} = \frac{N}{2\pi}\int_{\text{period}} \frac{ds}{\beta_u(s)} = \frac{N\mu_u}{2\pi} \tag{8.16}$$

DRAFT

Weak focusing approximation

In a cylindrically symmetric structure the sinusoidal motion is the exact solution of the first order differential equations of motion (Eqs. 3.16, 3.17, Classical Cyclotron chapter), the coefficients $K_x = (1-n)/\rho_0^2$ and $K_y = n/\rho_0^2$ are independent of s. Adding drift spaces results in Hill's differential equation with periodic coefficient $K(s+S) = K(s)$ (Eq. 8.11), with solution a pseudo harmonic motion (Eq. 8.14). Due to the weak focusing the beam envelope is only weakly modulated (*cf.* below), thus also is $\beta_u(s)$. In practice the modulation of $\beta_u(s)$ does not exceed a few percent, justifying the introduction of the average value $\overline{\beta_u}$ to approximate the phase advance by

$$\int_0^s \frac{ds}{\beta_u(s)} \approx \frac{s}{\overline{\beta_u}} = \nu_u \frac{s}{R} \tag{8.17}$$

The right equality is obtained by applying this approximation to the phase advance per period, namely

$$\mu_u = \int_{s_0}^{s_0+S} \frac{ds}{\beta_u(s)} \approx \frac{S}{\overline{\beta_u}} \tag{8.18}$$

and introducing the wave number of the N-period optical structure (Eq. 8.16) so that

$$\overline{\beta_u} = \frac{R}{\nu_u} \tag{8.19}$$

the wavelength of the betatron oscillation. With $k \ll 1$ and using Eq. 8.23,

$$\overline{\beta_x} = \frac{\rho_0(1+k/2)}{\sqrt{1-n}}, \quad \overline{\beta_y} = \frac{\rho_0(1+k/2)}{\sqrt{n}} \tag{8.20}$$

Substituting $\nu_u \frac{s}{R}$ to $\int \frac{ds}{\beta_u(s)}$ in Eq. 8.14 yields the approximate solution

$$\begin{cases} u(s) \approx \sqrt{\beta_u(s)\varepsilon_u/\pi}\, \cos\left(\nu_u \frac{s}{R} + \phi\right) \\ u'(s) \approx -\sqrt{\frac{\varepsilon_u/\pi}{\beta_u(s)}}\, \sin\left(\nu_u \frac{s}{R} + \phi\right) + \alpha_u(s)\, \cos\left(\nu_u \frac{s}{R} + \phi\right) \end{cases} \tag{8.21}$$

Beam envelopes

The beam envelope $\hat{u}(s)$ (with u standing for x or y) is determined by a particle on the maximum invariant ε_u/π. It is given at all s by

$$\hat{u}(s) = \pm\sqrt{\beta_u(s)\frac{\varepsilon_u}{\pi}} \tag{8.22}$$

As $\beta_u(s)$ is S-periodic, so also is the envelope, $\hat{u}(s+S) = \hat{u}(s)$. In a cell with symmetries, the beam envelopes feature the same symmetries, as shown in Fig. 8.10

DRAFT

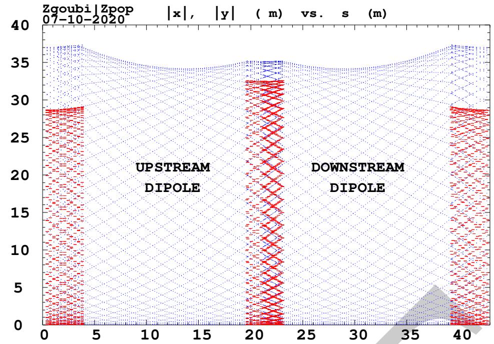

Fig. 8.10 Multiturn particle excursion (absolute values, $|x(s)|$ and $|y(s)|$) along the ZGS 2-dipole 43 m cell. The motion extrema ($[\beta_\mathrm{u}(s)\varepsilon_\mathrm{u}/\pi]^{1/2}$, Eq. 8.22) tangent the envelops, respectively horizontal (red, across the dipoles), and vertical (blue). Envelops are only weakly modulated. They feature the symmetry of the cell

for the ZGS: a symmetry with respect to the center of the cell. Envelope extrema are at azimuth s of $\beta_\mathrm{u}(s)$ extrema, *i.e.* where $d\hat{u}(s)/ds \propto \beta'_\mathrm{u}(s) = 0$ or $\alpha_\mathrm{u} = 0$ as $\beta'_\mathrm{u} = -2\alpha_\mathrm{u}$.

Working point

The "working point" of the synchrotron is the wave number pair (ν_x, ν_y) at which the accelerator is operated, it fully characterizes the focusing. In a structure with cylindrical symmetry (such as the classical cyclotron) $\nu_x = \sqrt{1-n}$ and $\nu_y = \sqrt{n}$ (Eq. 3.18) so that $\nu_x^2 + \nu_y^2 = 1$: when the radial field index n is changed the working point stays on a circle of radius 1 in the stability diagram (or "tune diagram", Fig. 8.11). If drift spaces are added, from Eqs. 8.19, 8.20, with $1 + \frac{k}{2} \approx \sqrt{R/\rho_0}$

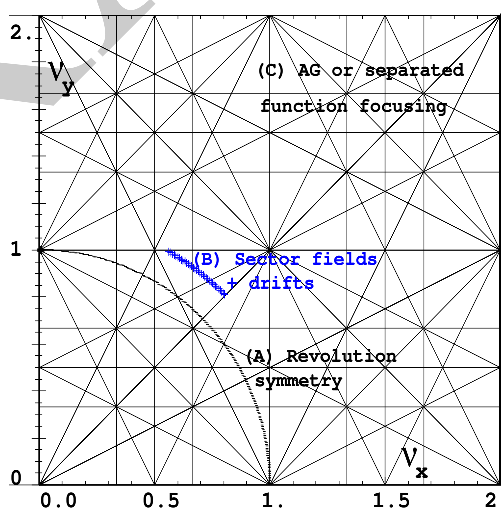

Fig. 8.11 Location of the working point in the tune diagram. (A) field with revolution symmetry: (ν_x, ν_y) is on a circle of radius 1; (B) sector field with index $0 < n < 1$ and drift spaces: (ν_x, ν_y) is on a circle of radius $\sqrt{R/\rho_0}$; (C) strong focusing, AG index $|n| \gg 1$ or separated function: ν_x and ν_y are large, set independently

DRAFT

(Eq. 8.6), it comes

$$\nu_x \approx \sqrt{(1-n)\frac{R}{\rho_0}}, \quad \nu_y \approx \sqrt{n\frac{R}{\rho_0}}, \qquad \nu_x^2 + \nu_y^2 \approx \frac{R}{\rho_0} \tag{8.23}$$

Thus the working point is located on a circle of radius $\sqrt{R/\rho_0} > 1$ (Fig. 8.11), tunes can not exceed the limits

$$0 < \nu_{\mathrm{x,\,y}} \lesssim \sqrt{R/\rho_0}$$

Horizontal and vertical focusing are not independent (Eq. 8.11): if ν_x increases then ν_y decreases and vice versa. This is a lack of flexibility which strong focusing overcomes by providing two knobs allowing separate adjustment.

Off-momentum orbits; *periodic dispersion*

In the linear approximation in $\Delta p/p_0$, a momentum offset $\Delta p = p - p_0$ changes mv to $mv(1+\Delta p/p_0)$ in Eq. 8.8. This changes the horizontal equation of motion (Eq. 8.10) to

$$\frac{d^2x}{ds^2} + K_x x = \frac{1}{\rho_0}\frac{\Delta p}{p_0}, \quad \text{or} \quad \frac{d^2x}{ds^2} + K_x\left(x - \frac{1}{\rho_0 K_x}\frac{\Delta p}{p_0}\right) = 0 \tag{8.24}$$

A change of variable $x - \frac{1}{K_x\rho_0}\frac{\Delta p}{p_0} \to x$ (with $1/\rho_0 K_x = \rho_0/(1-n)$) restores the unperturbed equation of motion; thus orbits of different momenta $p = p_0 + \Delta p$ are separated by

$$\Delta x = \frac{\rho_0}{1-n}\frac{\Delta p}{p_0} \tag{8.25}$$

from the reference orbit (Fig. 8.12). Introducing the geometrical radius $R = (1+k)\rho_0$

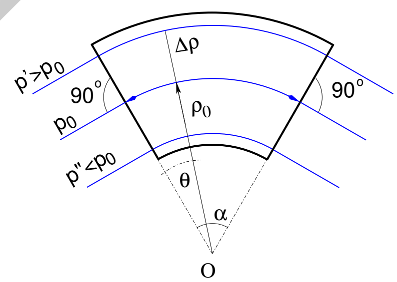

Fig. 8.12 In a sector dipole with radial index $n \neq 0$, closed orbits follow arcs of constant field. A closed orbit at $p_0 + \Delta p$ follows an arc of radius $\rho_0 + \Delta\rho$, $\Delta\rho = \Delta p/(1-n)qB_0$

(Eq. 8.6) to account for the added drifts, this yields the dispersion function

$$D_x = \frac{\Delta x}{\Delta p/p_0} \equiv \frac{\Delta R}{\Delta p/p_0} = \frac{R}{(1-n)(1+k)} = \frac{\rho_0}{1-n}, \quad \text{constant, positive} \tag{8.26}$$

DRAFT

D_x is the chromatic dispersion of the orbits, an s-independent quantity: in a structure with axial symmetry, comprising drift sections (Fig. 8.5) or not (classical and AVF cyclotrons for instance), the ratio $\Delta x \,/\, \Delta p/p_0$ is independent of the azimuth s, the distance of a chromatic orbit to the reference orbit is constant around the ring.

Given that $n < 1$,
- higher momentum orbits, $p > p_0$, have a greater radius,
- lower momentum orbits, $p < p_0$, have a smaller radius.

The horizontal motion of an off-momentum particle is a superposition of the betatron motion (solution of Hill's Eq. 8.21 taken for $u = x$) and of a particular solution of the inhomogeneous equation (Eq. 8.24), namely

$$x(s) = \sqrt{\beta_\mathrm{u}(s)\varepsilon_\mathrm{u}/\pi}\,\cos\left(\nu_\mathrm{u}\frac{s}{R} + \phi\right) + \frac{\rho_0}{1-n}\frac{\Delta p}{p_0} \tag{8.27}$$

The vertical motion is unchanged.

Chromatic orbit length

In an axially symmetric structure the difference in closed orbit length $\Delta C = 2\pi\Delta R$ resulting from the difference in momentum comes from the dipoles, as all orbits are parallel in the drifts (Fig. 8.5). Hence, from Eq. 8.26, the relative closed orbit lengthening factor, or momentum compaction, is

$$\alpha = \frac{\Delta C}{C}\Big/\frac{\Delta p}{p_0} \equiv \frac{\Delta R}{R}\Big/\frac{\Delta p}{p_0} = \frac{1}{(1-n)(1+k)} \approx \frac{1}{\nu_x^2} \tag{8.28}$$

with $k = Nl/\pi\rho_0$ (Eq. 8.6). Note that the relationship $\alpha \approx 1/\nu_x^2$ between momentum compaction and horizontal wave number established for a revolution symmetry structure (Eq. 3.22) still holds when adding drifts.

8.2.2 Acceleration

The field B in a synchrotron is varied during acceleration (a function performed by the magnet power supply) concurrently with the variation of the bunch momentum p (a function performed by the accelerating cavity) in such a way that the beam stays on the design orbit. Given the energies involved, the magnet supply imposes its law $B(t)$ (Fig. 8.13), and the cavity follows the best it can. The accelerating voltage $\hat{V}(t) = \sin\omega_\mathrm{rf}t$ is maintained in synchronism with the revolution motion by ensuring, as well as possible,

$$\omega_\mathrm{rf} = h\omega_\mathrm{rev} = h\frac{c}{R}\frac{B(t)}{\sqrt{\left(\frac{m_0 c}{q\rho}\right)^2 + B^2(t)}}$$

DRAFT

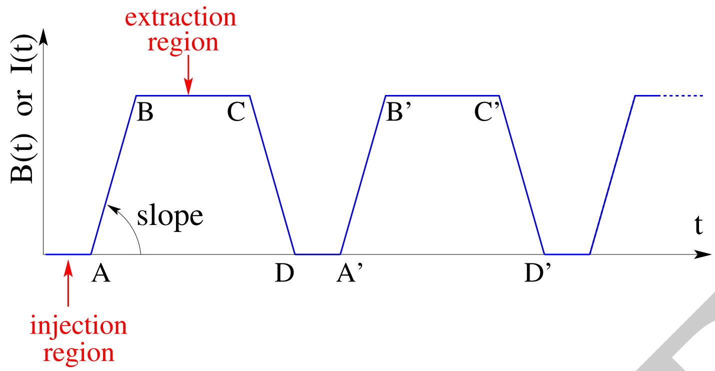

Fig. 8.13 Cycling $B(t)$ in a pulsed synchrotron. Ignoring saturation, $B(t)$ during the ramp is proportional to the magnet power supply current $I(t)$. Beam injection occurs at low field, in the region of A, while extraction occurs at top energy on the high field plateau. (AB): field ramp up (acceleration); (BC): flat top; (CD): field ramp down; (DA'): thermal relaxation. (AA'): repetition period; (1/AA'): repetition rate; *slope*: ramp velocity $\dot{B} = dB/dt$ (T/s)

Typically, for a $C = 2\pi R \approx 70$ m circumference ring[5], accelerating from $\beta = v/c \approx 0.09$ at injection (3.6 MeV protons) to $\beta \approx 1$ at top energy (3 GeV), the revolution period $T_{\rm rev} = C/\beta c$ and frequency $\omega_{\rm rev}/2\pi = 1/T_{\rm rev}$ span

$$\begin{cases} T_{\rm rev} : \ 2.6\,\mu\text{s} \ \rightarrow \ 0.24\,\mu\text{s} \\ f_{\rm rev} : \ 380\,\text{kHz} \rightarrow 4.2\,\text{MHz} \end{cases}$$

Energy gain

The variation of the particle energy over one turn amounts to the work of the force $F = dp/dt = q\rho dB/dt$ on the charge at the cavity, namely

$$\Delta W = F \cdot 2\pi R = 2\pi R q \rho \dot{B} \tag{8.29}$$

In a slow-cycling synchrotron $\dot{B}$ is usually constant over most of the acceleration cycle (Eq. 8.3), and so is ΔW. At SATURNE 1, for instance

$$\frac{\Delta W}{q} = 2\pi R \rho \dot{B} = 68.9_{[\rm m]} \times 8.42_{[\rm m]} \times 1.8_{[\rm T/m]} = 1044\ \text{volts/turn}$$

The field ramp lasts

$$\Delta t = (B_{\rm max} - B_{\rm min})/\dot{B} \approx B_{\rm max}/\dot{B} = 0.8\ \text{s}$$

The number of turns to the top energy ($W_{\rm max} \approx 3$ GeV) is

[5] Case of the SATURNE 1 weak focusing synchrotron (Fig. 8.1), *cf.* Exercise 8.1, Tab. 8.1

DRAFT

$$N = \frac{W_{\max}}{\Delta W} = \frac{3\,10^9 \text{ eV}}{1044 \text{ eV/turn}} \approx 3\,10^6 \text{turns}$$

The dependence of particle mass on field writes

$$m(t) = \gamma(t) m_0 = \frac{q\rho}{c}\sqrt{\left(\frac{m_0 c}{q\rho}\right)^2 + B^2(t)}$$

5025 *Adiabatic damping of the betatron oscillations*

Particle momentum increases at the accelerating gap, resulting in a decrease of the amplitude of betatron oscillations (an increase if deceleration). The mechanism is sketched in Fig. 8.14 (the solution of the equations of motion is addressed in Sect. 10.2.3). The slope at the cavity is

$$\text{before the cavity: } \frac{du}{ds} = \frac{m\frac{du}{dt}}{m\frac{ds}{dt}} = \frac{p_\mathrm{u}}{p_\mathrm{s}}, \qquad \text{after: } \left.\frac{du}{ds}\right|_2 = \left.\frac{m\frac{du}{dt}}{m\frac{ds}{dt}}\right|_2 = \frac{p_{\mathrm{u},2}}{p_{\mathrm{s},2}}$$

with u standing for x or y. As the kick in momentum is longitudinal, $dp_\mathrm{u}/dt = 0$

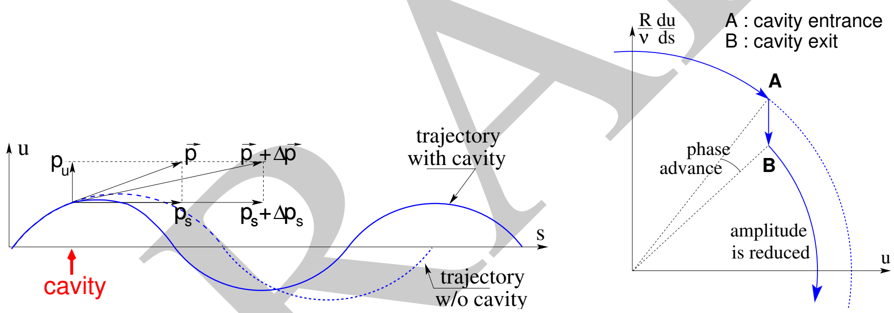

Fig. 8.14 Adiabatic damping of betatron oscillations from $u' = p_\mathrm{u}/p_\mathrm{s}$ to $u'_2 = p_\mathrm{u}/(p_\mathrm{s} + \Delta p_\mathrm{s})$ at the accelerating cavity. In transverse phase space the particle motion invariant ε_u decreases, as a result of $\Delta\left(\frac{du}{ds}\right)$

thus $p_{\mathrm{u},2} = p_\mathrm{u}$ and the increase in momentum is purely longitudinal, $p_{\mathrm{s},2} = p_\mathrm{s} + \Delta p_s$. Thus

$$\left.\frac{du}{ds}\right|_2 = \frac{p_\mathrm{u}}{p_\mathrm{s} + \Delta p_s} \approx \frac{p_\mathrm{u}}{p_\mathrm{s}}\left(1 - \frac{\Delta p_s}{p_\mathrm{s}}\right)$$

and as a consequence the slope du/ds varies across the cavity,

$$\Delta\left(\frac{du}{ds}\right) = \left.\frac{du}{ds}\right|_2 - \frac{du}{ds} = -\frac{du}{ds}\frac{\Delta p_\mathrm{s}}{p_\mathrm{s}}, \qquad \text{proportional to the slope}$$

DRAFT

If $\Delta p/p > 0$ (acceleration) then the slope decreases. This variation has two consequences on the betatron oscillation (Fig. 8.14):

- a change of the betatron phase,
- a modification of the betatron amplitude.

Coordinate transport

At the cavity

$$\begin{cases} u_2 = u \\ u'_2 \approx \frac{p_\mathrm{u}}{p_\mathrm{s}}(1 - \frac{dp}{p}) = u'(1 - \frac{dp}{p}) \end{cases}$$

In matrix form,

$$\begin{pmatrix} u_2 \\ u'_2 \end{pmatrix} = [C]\begin{pmatrix} u \\ u' \end{pmatrix} \quad \text{with} \quad [C] = \begin{bmatrix} 1 & 0 \\ 0 & 1 - \frac{dp}{p} \end{bmatrix} \tag{8.30}$$

Since $det[C] = 1 - \frac{dp}{p} \neq 1$ the system is non-conservative and the area of the beam ellipse in phase space is not conserved. Assume one cavity in the ring and note $[T] \times [C]$ the one-turn coordinate transport matrix with origin at entrance of the cavity. Its determinant is

$$det[T] \times det[C] = det[C] = 1 - \frac{dp}{p}$$

The variation of the transverse ellipse area satisfies $\varepsilon_\mathrm{u} = (1 - \frac{dp}{p_0})\varepsilon_0$ or, with $d\varepsilon_\mathrm{u} = \varepsilon_\mathrm{u} - \varepsilon_0$, $\frac{d\varepsilon_\mathrm{u}}{\varepsilon_\mathrm{u}} = -\frac{dp}{p_0}$, The solution is

$$p\ \varepsilon_\mathrm{u} = \text{constant}, \quad \text{or} \quad \beta\gamma\varepsilon_\mathrm{u} = \text{constant} \tag{8.31}$$

Over N turns the coordinate transport matrix is $[T_N] = ([T][C])^N$, thus the ellipse area changes by a factor

$$det[C]^N = (1 - \frac{dp}{p})^N \approx 1 - N\frac{dp}{p}$$

Phase stability

The motion of a particle in the longitudinal phase space $(\phi, \delta p/p)$ is stabilized in the vicinity of a synchronous phase, ϕ_s, by the mechanism of phase stability, or longitudinal focusing (Fig. 8.15). It requires

(i) the presence of an RF cavity with frequency locked on the revolution time,

(ii) bunch centroid to be positioned either on the rising slope of the oscillating voltage (low energy regime), or on the falling slope (high energy regime).

DRAFT

The synchronous particle follows the reference closed orbit, its velocity satisfies $v(t) = \frac{qB\rho(t)}{m}$. At each turn it reaches the accelerating gap when the oscillating voltage is at the synchronous phase ϕ_s, and undergoes an energy gain

$$\Delta W = q\hat{V} \sin \phi_s$$

The condition $|\sin \phi_s| < 1$ imposes a lower limit to the cavity voltage for acceleration to happen. According to Eq. 8.29,

$$\hat{V} > 2\pi R \rho \dot{B}$$

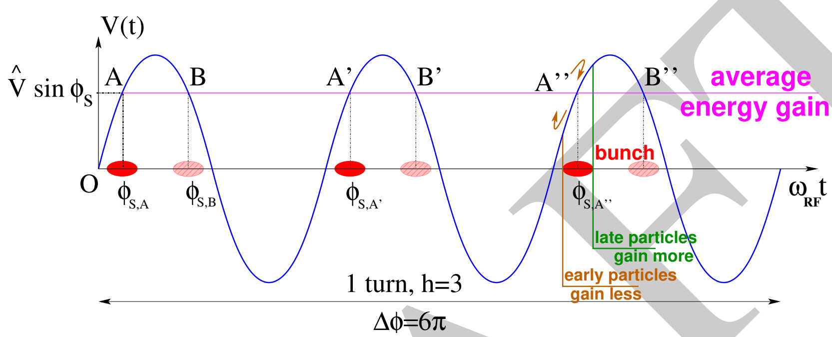

Fig. 8.15 A sketch of the mechanism of phase stability, $h = 3$ in this example. Below transition phase stability occurs for a synchronous phase taken at either one of A, A', A" arrival times at the gap. Beyond transition the stable phase is at either one of B, B', B' locations.

Referring to Fig. 8.15, the synchronous phase can be placed on the left (A, A', A" ... series) or on the right (B, B', B" ... series) of the oscillating voltage crest. One and only one of these two possibilities, and which one depending upon the optical lattice and on particle energy, ensures that particles in a bunch remain grouped in the vicinity of the synchronous particle.

The transition is between these two time-of-flight regimes. Consider a particle with higher energy compared to the synchronous particle:

- if the increase in path length around the ring is faster than the increase in velocity (case of classical cyclotron and synchrocyclotron; and of high energy electron synchrotron, where velocity essentially does not change), a revolution around the ring takes more time, the particle arrives at the accelerating gap late ($\phi(t) > \phi_s$); in order for it to be pulled toward bunch center (*i.e.*, take less time around the ring) it has to lower its energy increase; this is the B series, above transition;

- if the velocity increase is faster than the path length increase (case in general of synchrotrons at low energy), revolution around the ring takes less time, the particle arrives at the accelerating gap early ($\phi(t) < \phi_s$); in order for it to be pulled toward bunch center (*i.e.*, take more time around the ring) it has to lower its energy increase; this is the A series, below transition.

DRAFT

Transition energy

The transition between the two time-of-flight regimes occurs when $\frac{dT_{\rm rev}}{T_{\rm rev}} = 0$. With $T = 2\pi/\omega = C/v$, this can be written

$$\frac{d\omega_{\rm rev}}{\omega_{\rm rev}} = -\frac{dT_{\rm rev}}{T_{\rm rev}} = \frac{dv}{v} - \frac{dC}{C}$$

With $\frac{dv}{v} = \frac{1}{\gamma^2}\frac{dp}{p}$ and momentum compaction $\alpha = \frac{dC}{C} / \frac{dp}{p}$, (Eq. 8.28), it becomes

$$\frac{d\omega_{\rm rev}}{\omega_{\rm rev}} = -\frac{dT_{\rm rev}}{T_{\rm rev}} = \left(\frac{1}{\gamma^2} - \alpha\right)\frac{dp}{p} = \eta\frac{dp}{p} \tag{8.32}$$

which introduces the phase slip factor

$$\eta = \overbrace{\frac{1}{\gamma^2}}^{\text{kinematics}} - \underbrace{\alpha}_{\text{lattice}} = \frac{1}{\gamma^2} - \frac{1}{\gamma_{\rm tr}^2} \tag{8.33}$$

The "transition gamma", $\gamma_{\rm tr}$, is a property of the lattice.

In a weak focusing lattice, after Eq. 8.28 and classical cyclotron's Eq. 3.22,

$$\gamma_{\rm tr} = 1/\sqrt{\alpha} \approx \nu_x \tag{8.34}$$

Thus the phase stability regime is

$$\begin{aligned} &\text{below transition, } \textit{i.e. } \phi_{\rm s} < \pi/2, \quad \text{if} \quad \gamma < \nu_x \\ &\text{above transition, } \textit{i.e.} \phi_{\rm s} > \pi/2, \quad \text{if} \quad \gamma > \nu_x \end{aligned} \tag{8.35}$$

In a weak focusing synchrotron the horizontal tune $\nu_x = \sqrt{(1-n)R/\rho_0}$ (Eq. 8.23) may be $\gtrless 1$, and subsequently $\gamma_{\rm tr} > 1$ is a possibility, $\gamma_{\rm tr}$ may have to be crossed during acceleration. There is no transition gamma if $\nu_x < 1$. At SATURNE 1 for instance, with $\nu_x \approx 0.7$ (Tab. 8.1) and $\gamma_{\rm tr} < 1$. So, ramping in energy did not require crossing transition-gamma[6].

8.2.3 Synchrotron Radiation Poynting

Visible SR was first observed in the GEC 70 MeV weak focusing synchrotron [4]. So, the bases of SR theory may opportunistically be recalled here [26, 27]. This

[6] Transition-γ crossing (Sect. 8.2.2) is a common longitudinal phase space beam manipulation during acceleration in strong focusing synchrotrons. It requires an RF phase jump [25].

DRAFT

theoretical material serves the purpose of the exercises in addition. The topic is further explored in Sect. 9.2.6, which addresses some aspects of the use of visible SR for high energy electron or proton beam imaging.

In addressing low energy SR, the Poynting vector

$$\mathbf{P} = \mathbf{E} \times \mathbf{B}$$

is the relevant quantity [27, 28]. The electromagnetic field is given by the Liénard-

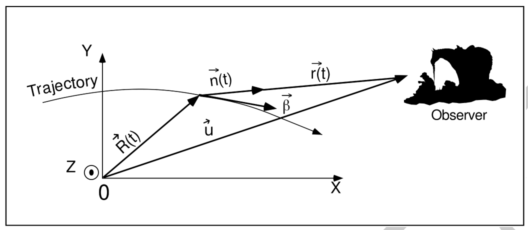

Fig. 8.16 The frame and vectors entering in the definition of the electric field radiated by the accelerated particle (Eq. 8.36). `Zgoubi` notations are used here (Fig. 1.3): (X, Y): horizontal plane; Z: vertical axis; $\mathbf{R}(t)$ is the particle position in the laboratory frame (O, X, Y, Z). Besides, $\mathbf{u}$ is the position of the observer; $\mathbf{r}(t) = \mathbf{u} - \mathbf{R}(t)$ is the position of the particle with respect to the observer; $\mathbf{n}(t) = \mathbf{r}(t)/|\mathbf{r}(t)|$ is the (normalized) direction of observation; $\boldsymbol{\beta} = (1/c)d\mathbf{R}/dt$ is the normalized velocity vector of the particle

Wiechert equations in the long distance approximation

$$\mathbf{E}(\mathbf{n}, \tau) = \frac{q}{4\pi\varepsilon_0 c} \frac{\mathbf{n}(t) \times [(\mathbf{n}(t) - \boldsymbol{\beta}(t)) \times d\boldsymbol{\beta}/dt]}{r(t)\,(1 - \mathbf{n}(t) \cdot \boldsymbol{\beta}(t))^3}, \qquad \mathbf{B} = \frac{1}{c}\mathbf{n} \times \mathbf{E} \tag{8.36}$$

where $\mathbf{n} = \mathbf{r}/r$ is the direction of observation (Fig. 8.16), $\boldsymbol{\beta} = \mathbf{v}/c$, $\dot{\boldsymbol{\beta}} = d\boldsymbol{\beta}/dt$, t is the "retarded time", at which the particle emitted the radiation, τ is the observer time, a little later. Namely, when at position $\mathbf{r}(t)$ with respect to the observer, the particle emits a signal which reaches the observer at time

$$\tau = t + r(t)/c \tag{8.37}$$

Electric impulse, From Raytracing [29*, Sect.* 3.2.1]

The vectors $\mathbf{n}$, $\boldsymbol{\beta}$, $\dot{\boldsymbol{\beta}}$ are sub-products of the stepwise integration of particle motion. They are used to compute $\mathbf{E}(\mathbf{n}, \tau)$ in `zpop` (its subroutine sref.f, actually).

The electric field impulse $\mathbf{E}(\mathbf{n}, \tau)$ is decomposed into two polarization components $E_\sigma(\mathbf{n}, \tau)$ and $E_\pi(\mathbf{n}, \tau)$, respectively parallel and normal to the bend plane (Fig. 8.17).

As an example, results for GEC 70 MeV synchrotron are given in Fig. 8.17: the electric field impulses have been derived from the electron trajectory ob-

DRAFT

tained by stepwise raytracing, using Eq. 8.36, 8.37. The spectral brightness follows, Eqs. 8.38, 8.39.

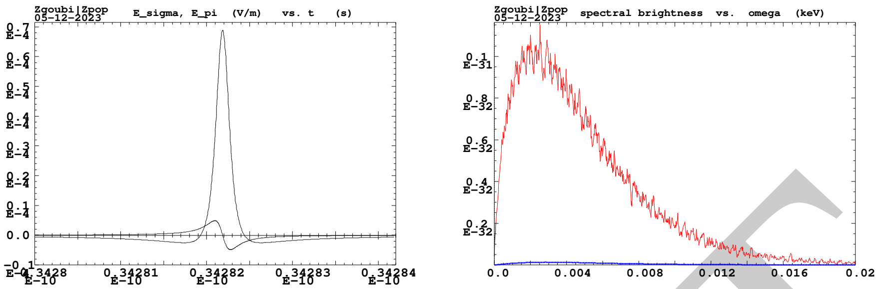

Fig. 8.17 Left: typical shape of $E_{\sigma,\,\pi}(\tau)$ impulses as observed in the direction $\phi = 0,\ \psi \approx 0.1/\gamma$, in GEC 70 MeV synchrotron (by comparison, at $\phi = \psi = 0$ $E_\sigma(\tau)$ is marginally different, whereas $E_\pi(\tau) \equiv 0$). Right: spectral brightness, peaking near $\hbar\omega_c = 2\gamma^3 c/2\rho \approx 2.7\,\mathrm{eV}$ ($\lambda_c = 0.47\,\mu\mathrm{m}$); at such small $\psi \approx 0.1/\gamma$, the π component of the radiation (blue curve) is quite weak compared to the σ component (red curve)

Spectral brightness [29*, Sect.* 3.2.2]

The respective Fourier transforms of the electric field impulse components $E_\sigma(\mathbf{n},\tau)$ and $E_\pi(\mathbf{n},\tau)$, namely

$$\tilde{E}_{\sigma,\,\pi}(\phi,\psi,\omega) = \int E_{\sigma,\,\pi}(\phi,\psi,t)e^{-i\omega\tau}\,d\tau\ /\ \sqrt{2\pi} \tag{8.38}$$

provide the spectral angular brightness (Fig. 8.17)

$$\frac{\partial^3 P_{\sigma,\pi}}{\partial\phi\partial\psi\partial\omega} = 2\epsilon_0 c r^2 \left|\tilde{E}_{\sigma,\,\pi}(\phi,\psi,\omega)\right|^2 \tag{8.39}$$

with ϕ and ψ the angles of $\mathbf{n}$ to respectively the (X,Z) and (X,Y) planes. Zpop computes $\tilde{E}_{\sigma,\,\pi}(\phi,\psi,\omega)$ and $\frac{\partial^3 P_{\sigma,\pi}}{\partial\phi\partial\psi\partial\omega}$ (its subroutine srdw.f, actually).

Electric impulse, Analytical [27] [29*, Sect.* 3.2]

The following theoretical reminders are resorted to in the exercises, for instance for comparison to numerical outcomes from the computation of the electric impulse $\mathbf{E}(\mathbf{n},\tau)$ (Eq. 8.36) from numerical integration. Referring to Fig. 8.16, the observer direction and velocity vectors write

$$\mathbf{n} = (\cos\psi\cos\phi, \cos\psi\sin\phi, \sin\psi), \quad \boldsymbol{\beta} = \beta(\cos\omega_0 t, \sin\omega_0 t, 0) \tag{8.40}$$

DRAFT

The observer time τ and, to order $1/\gamma^2$, its differential element are obtained from the particle time t (the numerical integration time) using

$$\tau = \frac{1+\gamma^2\psi^2}{2\gamma^2}t + \frac{\omega_0^2}{6}t^3, \quad \frac{d\tau}{dt} = 1 - \mathbf{n}(t)\cdot\boldsymbol{\beta}(t) \simeq \frac{1+\gamma^2\psi^2}{2\gamma^2} + \frac{1}{2}(\omega_0 t - \phi)^2 \tag{8.41}$$

with $\omega_0 \approx c/\rho$ and ρ the local curvature radius. The origin of observer time is at $\phi = \psi = 0$, *i.e.* in the direction tangent to particle trajectory. The radiated electric impulses result, namely

$$\begin{aligned} E_\sigma(t) &= \frac{q\omega_0\gamma^4}{\pi\epsilon_0 cr}\frac{(1+\gamma^2\psi^2) - \gamma^2(\omega_0 t-\phi)^2}{\left(1+\gamma^2\psi^2+\gamma^2(\omega_0 t-\phi)^2\right)^3}\mathrm{rect}\left(\frac{t}{2T}\right) \\ E_\pi(t) &= \frac{q\omega_0\gamma^4}{\pi\epsilon_0 cr}\frac{-2\gamma\psi\gamma(\omega_0 t-\phi)}{\left(1+\gamma^2\psi^2+\gamma^2(\omega_0 t-\phi)^2\right)^3}\mathrm{rect}(\frac{t}{2T}) \end{aligned} \tag{8.42}$$

where $\mathrm{rect}(x) = 1$ if $-\frac{1}{2} < x < \frac{1}{2}$, zero otherwise, defines the boundary of the numerical integration, namely over a particle deviation angle $\alpha = \pm\omega_0 T$. The impulse components $E_{\sigma,\pi}(t)$ in particle time have similar shapes to $E_{\sigma,\pi}(\tau)$ at the observer, Eq. 8.43 (Fig. 8.17), they differ in width as the latter is squeezed according to $\tau(t)$ contraction (Eq. 8.41) - a squeeze resulting from a double Doppler shift from electron trajectory arc in the lab, to electron frame, and back to observed radiation in the lab, $\Delta\tau \approx \Delta t/\gamma^2$. The cubic dependence $\tau(t)$ (Eq. 8.41) has an analytical solution; substitution of that solution $t(\tau)$ in Eq. 8.42 yields analytical expressions for the field impulses in observer time,

$$\begin{aligned} E_\sigma(\phi,\psi,\tau) &= \frac{q\omega_0\gamma^4}{\pi\epsilon_0 cr}\frac{1-4\,\mathrm{hsin}^2[\frac{1}{3}\mathrm{Ahsin}\,u(\phi,\psi,\tau)]}{(1+\gamma^2\psi^2)^2(1+4\,\mathrm{hsin}^2[\frac{1}{3}\mathrm{Ahsin}\,u(\phi,\psi,\tau)])^3}\mathrm{rect}[\frac{\tau}{2\Gamma(\phi,\psi)}] \\ E_\pi(\phi,\psi,\tau) &= \frac{q\omega_0\gamma^4}{\pi\epsilon_0 cr}\frac{4\gamma\psi\ \mathrm{hsin}[\frac{1}{3}\mathrm{Ahsin}\,u(\phi,\psi,\tau)]}{(1+\gamma^2\psi^2)^{5/2}(1+4\,\mathrm{hsin}^2[\frac{1}{3}\mathrm{Ahsin}\,u(\phi,\psi,\tau)])^3}\mathrm{rect}[\frac{\tau}{2\Gamma(\phi,\psi)}] \end{aligned} \tag{8.43}$$

where $\Gamma(\phi,\psi)$ is the observation direction dependent signal duration and $u = \frac{1}{2}\frac{\gamma\phi}{\sqrt{1+\gamma^2\psi^2}}\left(3+\frac{\gamma^2\phi^2}{1+\gamma^2\psi^2}\right) - 2\frac{\omega_c}{(1+\gamma^2\psi^2)^{3/2}}\tau$. The critical frequency ω_c partitions the power spectrum in two equal parts, $\int_0^{\omega_c}\frac{dP}{d\omega} = \int_{\omega_c}^{\infty}\frac{dP}{d\omega}$. Equation 8.43 can be used to check numerical integration outcomes. Refer to [26, Sect. 4.4][27] for additional details.

The typical width of the impulse in observer time is the familiar

$$\Delta\tau_c = \pm\frac{1}{\omega_c}\left(1+\gamma^2\psi^2\right)^{3/2} \quad \text{with} \quad \omega_c = \frac{3\gamma^3 c}{2\rho} \ \text{ the critical frequency} \tag{8.44}$$

Accounting for the γ^2 double Doppler shift contarction, $\Delta\tau_c$ thus corresponds to a trajectory arc length $l_c \approx c\Delta\tau_c \times \gamma^2 \approx \rho/\gamma$. From the point of view of the observer, the SR power, integrated over the all spectrum, is mostly contained in an *rms* opening angle [26, Sect. 5.5.2] (Fig. 8.18)

DRAFT

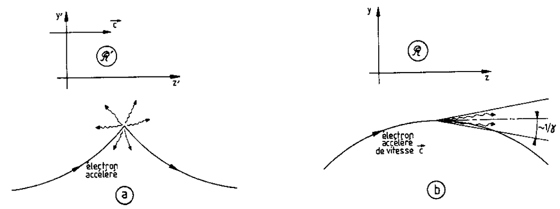

Fig. 8.18 Electron trajectory in the lab frame $\mathcal{R}$ (right) and in $\mathcal{R}'$ traveling parallel to, and at, its velocity (left). The radiation, spanning a $\pm pi/2$ angle in $\mathcal{R}'$, is confined in a forward cone of opening $\pm\Delta\phi_c \approx \pm 1/\gamma$ in $\mathcal{R}$

$$\Delta\phi_{c,\mathrm{rms}} = 0.83\frac{1}{\gamma} \tag{8.45}$$

For a given observation frequency ω, the *rms* opening angle is a function of frequency and satisfies [26, Sect. 5.5.1]

$$\Delta\phi_c(\omega) \approx 0.72\frac{1}{\gamma}\left(\frac{\omega_c}{\omega}\right)^{1/3} \tag{8.46}$$

Lower radiation energy has wider opening.

8.2.4 Depolarizing Resonances

The field index is zero in the ZGS, transverse focusing is ensured by wedge angles at the ends of the eight dipoles, the only locations where non-zero horizontal field components are present. The latter are weak and as a consequence so also are depolarizing resonances: *"As we can see from the table, the transition probability* [*from spin state* $\psi_{1/2}$ *to spin state* $\psi_{-1/2}$] *is reasonably small up to* $\gamma = 7.1$*"* [17], *i.e.* proton $G\gamma = 12.73$, $p = 6.6$ GeV/c. The table referred to stipulates a transition probability $P_{\frac{1}{2},-\frac{1}{2}} < 0.042$, whereas resonances beyond that energy range feature $P_{\frac{1}{2},-\frac{1}{2}} > 0.36$. Beam depolarization up to 6 GeV/c, under the effect of these resonances, is illustrated in Fig. 8.19.

In a synchrotron using gradient dipoles, particles experience radial fields $B_x(y) = -n\frac{B_0}{\rho_0}y$ as they undergo vertical betatron oscillations [17, 30, 31]. As n is small these radial field components are weak, and so is their effect on spin motion.

In a P-periodic ring, the vertical betatron motion excites "systematic intrinsic" spin resonances, located at

$$G\gamma_R = k\,P \pm \nu_y, \qquad k \in \mathbb{N}$$

If the P periodicity of the optics is lost (due to an optical defect), all resonances, systematic and non-systematic, $G\gamma_R$ = integer $\pm\,\nu_y$ are excited. In the ZGS for instance, $\nu_y \approx 0.8$ (Tab. 8.2), the ring is P = 4-periodic, thus $G\gamma_R = 4k \pm 0.8$. Strongest intrinsic resonances are located at

$$G\gamma_R = k\,m\,P \pm \nu_y$$

DRAFT

with m the number of cells per superperiod [32, Sect. 3.II]. In the ZGS, with m=2 the strongest resonances occur at (Fig. 8.19)

$$G\gamma_R = 2 \times 4k \pm 0.8 = 7.2\ (3.65\,\text{GeV/c});\ 8.8\ (4.51\,\text{GeV/c});\ 15.2\ (7.9\,\text{GeV/c});\ \ldots$$

In the presence of vertical orbit defects, non-zero transverse fields are experienced

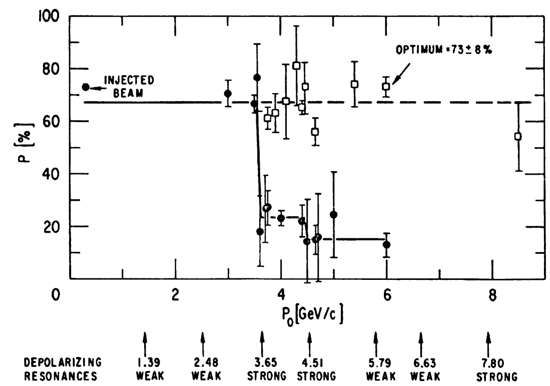

Fig. 8.19 Polarization loss at the ZGS [33] through the strong intrinsic resonances $G\gamma_R = 7.2$ ($p = 3.65$ GeV/c) and 8.8 (4.51 GeV/c) (black circles). A vertical tune jump method preserves polarization (empty circles)

along the closed orbit, they excite "imperfection", *aka* "integer", depolarizing resonances, located at

$$G\gamma_R = k, \qquad k \in \mathbb{N}$$

In the case that the periodicity of the orbit is that of the lattice, P, the sole imperfection resonances, located at $G\gamma_R = kP$, are excited. The strongest imperfection resonances are located at [32, Sect. 3.II]

$$G\gamma_R = k\, m\, P$$

Spin precession axis. Resonance width

Consider the spin vector

$$\mathbf{S}(\theta) = (S_\eta, S_\xi, S_y)$$

of a particle, in the laboratory frame, with θ the orbital angle around the accelerator. Introduce the projection $s(\theta)$ of $\mathbf{S}$ in the bend plane

$$s(\theta) = S_\eta(\theta) + jS_\xi(\theta) \qquad (\text{and } S_y^2 = 1 - s^2) \tag{8.47}$$

In the case of a stationary solution of the spin motion, viz. stationary spin precession axis around the ring (Fig. 8.21) [31, Sect. 3.6.1], s satisfies [31] (Fig. 8.20)

DRAFT

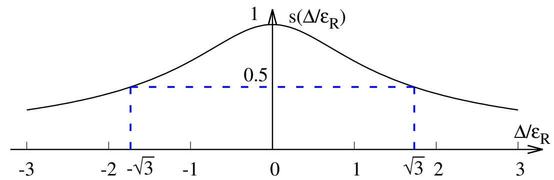

Fig. 8.20 A graph of $s(\Delta) = \sqrt{1 - S_y^2(\Delta)}$. $s = 1$ on the resonance ($\Delta = 0$), the spin vector lies in the bend plane. $s = 1/2$ at distance $\Delta = \pm\sqrt{3}\epsilon_R$ from $G\gamma_R$, the spin vector is at 30° to the y axis

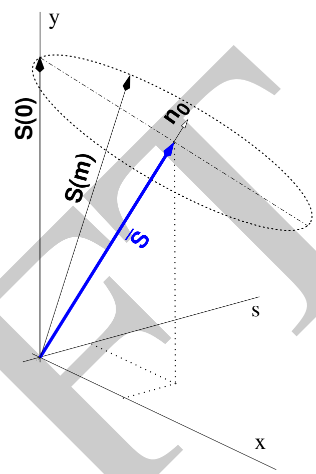

Fig. 8.21 Near an integer resonance, at any azimuth θ around the ring spins $\mathbf{S}(m)$ (m is the turn number, $\mathbf{S}(m)$ started vertical, here) precess at frequency $\omega = \sqrt{\Delta^2 + |\epsilon_R|^2}$ around a stationary axis $\mathbf{n}_0(\theta)$, whose orientation varies along the ring. $\mathbf{n}_0$ is aligned along $\overline{\mathbf{S}}$, average of $\mathbf{S}(m)$ over turns

$$s^2 = \frac{1}{1 + \dfrac{\Delta^2}{|\epsilon_R|^2}} \tag{8.48}$$

with $\Delta = G\gamma - G\gamma_R$ the distance to the resonance; thus the resonance width appears to be a measure of its strength. The quantity of interest is the angle, ϕ, of the spin

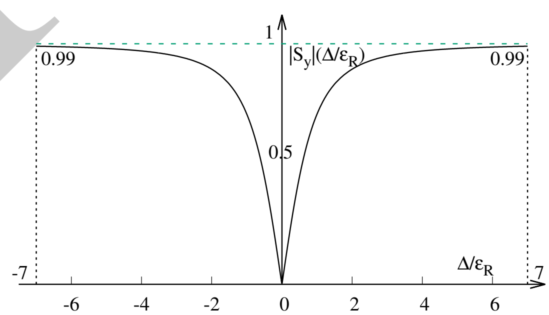

Fig. 8.22 Dependence of polarization on the distance to the resonance. For instance $|S_y| = 0.99$, 1% depolarization at $\Delta = \pm 7|\epsilon_R|$. $S_y = 0$, full depolarization on the resonance ($\Delta = 0$), the precession axis lies in the bend plane

precession direction to the vertical axis. It is given by (Fig. 8.22)

DRAFT

$$\cos^2 \phi(\Delta) \equiv S_y^2(\Delta) = 1 - s^2 = \frac{\Delta^2/|\epsilon_R|^2}{1 + \Delta^2/|\epsilon_R|^2} \tag{8.49}$$

On the resonance, with $\Delta = 0$, the spin precession axis lies in the bend plane: $\phi = \pm\pi/2$. A depolarization by 1% ($|S_y| = 0.99$) corresponds to a distance to the resonance $\Delta = 7|\epsilon_R|$, spin precession axis at an angle $\phi = \mathrm{acos}(0.99) = 8^o$ from the vertical.

Conversely,

$$\frac{\Delta^2}{|\epsilon_R|^2} = \frac{S_y^2}{1 - S_y^2} \tag{8.50}$$

The precession axis is common to all spins, while S_y is a measure of the polarization along the vertical axis,

$$S_y = \frac{N^+ - N^-}{N^+ + N^-}$$

where N^+ and N^- denote the number of particles in spin states $\frac{1}{2}$ and $-\frac{1}{2}$ respectively.

Things complicate a little in the vicinity of an intrinsic resonance [31, Sect. 3.6.2], the precession axis is not stationary, spins precess around it while it precesses itself around the vertical, Fig. 8.23.

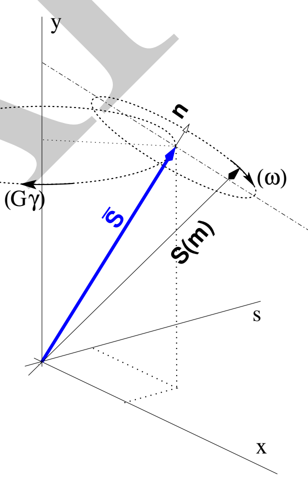

Fig. 8.23 Near an intrinsic resonance, spins $\mathbf{S}(m)$ precess at frequency ω around an axis $\mathbf{n}$, which itself precesses around the vertical axis at frequency $G\gamma$

Resonance crossing

Crossing an isolated resonance (Figs. 8.19, 8.24) polarization polarization according to the Froissart-Stora law [34] [31, Sect. 2.3.6],

$$\frac{P_f}{P_i} = 2e^{-\frac{\pi}{2}\frac{|\epsilon_R|^2}{\alpha}} - 1 \tag{8.51}$$

DRAFT

from a value P_i upstream to an asymptotic value P_f downstream of the resonance. In this expression

$$\alpha = G\frac{d\gamma}{d\theta} = \frac{1}{2\pi}\frac{\Delta E}{M} \tag{8.52}$$

is the crossing speed for an energy gain ΔE per turn.

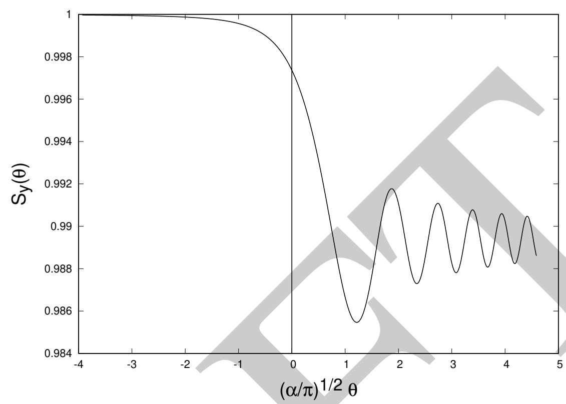

Fig. 8.24 Vertical component of spin motion $S_y(\theta)$ through a weak depolarizing resonance (Eq. 8.53). The vertical line is at the location of the resonance, which coincides with the origin of the orbital angle

Spin motion through weak resonances

Depolarizing resonances are weak up to several GeV in a weak focusing synchrotron because the radial and/or longitudinal fields are weak. Thus assume $S_{\mathrm{y,f}} \approx S_{\mathrm{y,i}}$, with $S_{\mathrm{y,f}}$ and $S_{\mathrm{y,i}}$ the asymptotic vertical spin component values respectively upstream and downstream of the resonance. With the origin of the orbital angle taken at the resonance (Fig. 8.24), and introducing the Fresnel integrals [31]

$$C(x) = \int_0^x \cos\left(\frac{\pi}{2}t^2\right)\, dt, \qquad S(x) = \int_0^x \sin\left(\frac{\pi}{2}t^2\right)\, dt$$

the polarization satisfies

$$\begin{aligned}
&\text{if } \theta < 0: \left(\frac{S_{\mathrm{y}}(\theta)}{S_{\mathrm{y,i}}}\right)^2 = 1 - \frac{\pi|\epsilon_R|^2}{\alpha}\left\{\left[\tfrac{1}{2} - C\left(-\theta\sqrt{\frac{\alpha}{\pi}}\right)\right]^2 + \left[\tfrac{1}{2} - S\left(-\theta\sqrt{\frac{\alpha}{\pi}}\right)\right]^2\right\}\\
&\text{if } \theta > 0: \left(\frac{S_{\mathrm{y}}(\theta)}{S_{\mathrm{y,i}}}\right)^2 = 1 - \frac{\pi|\epsilon_R|^2}{\alpha}\left\{\left[\tfrac{1}{2} + C\left(\theta\sqrt{\frac{\alpha}{\pi}}\right)\right]^2 + \left[\tfrac{1}{2} + S\left(\theta\sqrt{\frac{\alpha}{\pi}}\right)\right]^2\right\}
\end{aligned} \tag{8.53}$$

In the asymptotic limit,

$$\frac{S_{\mathrm{y}}(\theta)}{S_{\mathrm{y,i}}} \overset{\theta\longrightarrow\infty}{\longrightarrow} 1 - \frac{\pi}{\alpha}|\epsilon_R|^2 \tag{8.54}$$

DRAFT

which agrees with a Taylor development of Froissart-Stora formula, Eq. 8.51, to first order in $|\epsilon_R|^2/\alpha$. This approximation holds in the limit that higher order terms can be neglected.

DRAFT

8.3 Exercises

8.1 Construct SATURNE 1 synchrotron. Spin Resonances

Solution: page **??**.

In this exercise, the weak focusing 3 GeV synchrotron SATURNE 1 (Fig. 8.1) is modeled. Spin resonances in a weak dipole gradient lattice are observed.

Table 8.1 Parameters of SATURNE 1 weak focusing synchrotron [35]. ρ_0 denotes the reference bending radius in the dipole; the reference orbit, field index, wave numbers, etc., are taken along that radius

Orbit length, C	cm	6890
Average radius, $R = C/2\pi$	cm	1096.58
Drift length, $2l$	cm	400
Magnetic radius, ρ_0	cm	841.93
$R/\rho_0 = 1 + k$		1.30246
Field index n, nominal		0.6
Wave numbers ν_x, ν_y, nominal		0.72, 0.89
Stability limit		$0.5 < n < 0.757$
Injection energy (proton)	MeV	3.6
Field at injection	kG	0.326
Top energy	GeV	2.94
Field at top energy, $B_{\max}$	kG	14.9
$\dot{B}$	kG/s	18
Synchronous energy gain	keV/turn	1.160
RF harmonic		2

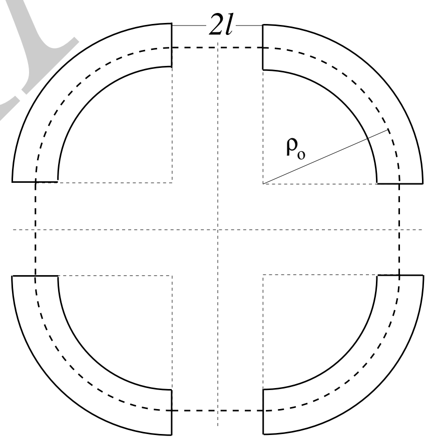

Fig. 8.25 A schematic layout of SATURNE 1, a $2\pi/4$ axial symmetry structure, comprised of 4 radial field index 90 deg dipoles and 4 drift spaces. The cell in the simulation exercises is taken as a $\pi/2$ quadrant: half-drift / 90^o-dipole / half-drift

(a) Construct a model of SATURNE 1 90^o cell dipole in the hard-edge model, using DIPOLE. Use the parameters given in Tab. 8.1, and Fig. 8.25 as a guidance. For beam monitoring purposes, split the dipole in two 45^o deg halves. It is judicious

DRAFT

to take RM=841.93 cm in DIPOLE, as this is the reference radius for the definition of the radial index. Take an integration step size in centimeter range - small enough to ensure numerical convergence, as large as doable for faster multiturn raytracing.

Validate the model by producing the 6×6 transport matrix of the cell dipole (MATRIX[IFOC=0] can be used for that, with OBJET[KOBJ=5] to define a proper set of paraxial initial coordinates) and checking against theory (Sect. 14.1, Eq. 14.7).

(b) Construct a model of SATURNE 1 cell, with origin at the center of the drift. Find the closed orbit, that particular trajectory which has all its coordinates zero in the drifts: use DIPOLE[KPOS] to cancel the closed orbit coordinates at DIPOLE ends. While there, check the expected value of the dispersion (Eq. 8.26) and of the momentum compaction (Eq. 8.28), from the raytracing of a chromatic closed orbit - *i.e.*, the orbit of an off-momentum particle. Plot these two orbits (on- and off-momentum), over a complete turn around the ring, on a common graph.

Compute the cell periodic optical functions and tunes, using either OBJET[KOBJ=5] and MATRIX[IORD=1,IFOC=11], or TWISS, or OBJET[KOBJ=6] and MATRIX[IORD=2,IFOC=11]; check their values against theory. Check consistency with previous dispersion function and momentum compaction outcomes.

Move the origin of the lattice at a different azimuth s along the cell: verify that, while the transport matrix depends on the origin, its trace does not.

Produce a graph of the optical functions (betatron functions and dispersion) along the cell. Check the expected average values of the betatron functions (Eq. 8.20).

Produce a scan of the tunes over the field index range $0.5 \leq n \leq 0.757$. REBELOTE[IOPT=1] can be used to repeatedly change n over that range. Superimpose the theoretical curves $\nu_x(n)$, $\nu_y(n)$.

(c) Justify considering the betatron oscillation as sinusoidal, namely,

$$y(\theta) = A\,\cos(\nu_y\theta + \phi)$$

wherein $\theta = s/R$, $R = \oint ds/2\pi$.

(d) Launch a few particles evenly distributed on a common paraxial horizontal Courant-Snyder invariant, vertical motion taken null (OBJET[KOBJ=8] can be used), for a single pass through the cell. Store particle data along the cell in zgoubi.plt, using DIPOLE[IL=2] and DRIFT[split,N=20,IL=2]. Use these to generate a graph of the beam envelopes.

Using Eq. 8.22 compare with the results obtained in (b). Find the minimum and maximum values of the betatron functions, and their azimuth $s(min[\beta_x])$, $s(max[\beta_x])$. Check the latter against theory.

Repeat for the vertical motion, taking $\varepsilon_x = 0$, ε_y paraxial.

Repeat, using, instead of several particles on a common invariant, a single particle traced over a few tens of turns.

(e) Produce an acceleration cycle from 3.6 MeV to 3 GeV, for a few particles launched on a common $10^{-4}\,\pi$m initial invariant in each plane. Ignore synchrotron motion (CAVITE[IOPT=3] can be used in that case). Take a peak voltage $\hat{V} = 200$ kV (for faster raytracing - unrealistic though, as it would result in prohibitive $\dot{B}$ (Eq. 8.29)) and synchronous phase $\phi_s = 150$ deg (justify $\phi_s > \pi/2$).

DRAFT

Check the betatron damping over the acceleration range: compare with theory (Eq. 8.31).

How close to symplectic the numerical integration is (it is by definition *not* symplectic, being a truncated Taylor series method [36, Eq. 1.2.4]), depends on the integration step size, and on the size of the flying mesh in the DIPOLE[IORDRE,Resol] method [36, Fig. 20]; check a possible departure of the betatron damping from theory as a function of these parameters.

Produce a graph of the horizontal and vertical wave number values over the acceleration cycle.

(f) Some spin motion, now. Adding SPNTRK at the beginning of the sequence used in (e) will ensure spin tracking.

Based on the input data file worked out for question (d), simulate the acceleration of a single particle, through the intrinsic resonance $G\gamma_R = 4 - \nu_y$, from a distance of a few times the resonance strength upstream (this requires determining BORO value under OBJET) to a distance of a few times the resonance strength downstream of the resonance, at an acceleration rate of 10 kV/turn.

OBJET[KOBJ=8] can be used to allow to easily define an initial invariant value.

Start with spin vertical. On a common graph, plot $S_y(turn)$ for a few different values of the vertical betatron invariant (the horizontal invariant value does not matter - explain that statement, it can be taken zero). Derive the resonance strength from this tracking, check against theory.

Repeat, for different crossing speeds.

Push the tracking beyond $G\gamma = 2{\times}4{+}\nu_y$: verify that the sole systematic resonances $G\gamma = \text{integer} \times P \pm \nu_y$ are excited - with $P = 4$ the periodicity of the ring.

Break the 4-periodicity of the lattice by perturbing the index in one of the 4 dipoles (say, by 10%), verify that all resonances $G\gamma = \text{integer} \pm \nu_y$ are now excited.

(g) Consider a case of weak resonance crossing, single particle (*i.e.*, a case where $P_f/P_i \approx 1$, taken from (f); crossing speed may be increased, or particle invariant decreased if needed), show that it satisfies Eq. 8.53. Match its turn-by-turn tracking data to Eq. 8.53 so to get the vertical betatron tune ν_y, the location of the resonance $G\gamma_{\mathrm{R}}$, and its strength.

(h) Stationary spin motion (*i.e.* at fixed energy) is considered in this question. Track a few particles with distances from the resonance $\Delta = G\gamma - G\gamma_R = G\gamma - (4 - \nu_y)$ evenly spanning the interval $\Delta \in [0, 7 \times \epsilon_R]$.

Produce on a common graph the spin motion $S_y(turn)$ for these particles, as observed at some azimuth along the ring.

Produce a graph of the average $_y$ over turns, $\langle S_y \rangle|_{\mathrm{turn}}(\Delta)$ (as in Fig. 8.22). Produce the vertical betatron tune ν_y, the location of the resonance $G\gamma_{\mathrm{R}}$, and its strength ϵ_R, obtained from a match of $\langle S_y \rangle|_{\mathrm{turn}}(\Delta)$ to (Eq. 8.49)

$$\langle S_y \rangle (\Delta) = \frac{|\Delta|}{\sqrt{|\epsilon_R|^2 + \Delta^2}}$$

(i) Track a 200-particle 6-D bunch, with Gaussian transverse densities $\varepsilon_{\mathrm{x,y}}$ a few μm, and Gaussian $\delta p/p$ with $\sigma_{\delta p/p} = 10^{-4}$. Produce a graph of the average value of

DRAFT

the vertical spin component S_y over a 200 particle set, as a function of $G\gamma$, across the $G\gamma_R = 4 - \nu_y$ resonance. Indicate on that graph the location of the resonant $G\gamma_R$ values.

Perform this resonance crossing for five different values of the particle invariant: $\varepsilon_y/\pi = 2,\ 10,\ 20,\ 40,\ 200\,\mu$m. Compute P_f/P_i in each case, check the dependence on ε_y against theory.

Compute the resonance strength, ε_y, from this tracking.

Re-do this crossing simulation for a different crossing speed (take for instance $\hat{V} = 10\,$kV) and a couple of vertical invariant values, compute P_f/P_i so obtained. Check the crossing speed dependence of P_f/P_i against theory.

8.2 Construct the ZGS synchrotron. Spin Resonances

Solution: page **??**.

In this exercise, the ZGS 12 GeV synchrotron is modeled. Spin resonances in a zero-gradient, wedge focusing synchrotron are addressed.

A photo taken in the ZGS tunnel is given in Fig. 8.4; a schematic layout of the ring is shown in Fig. 8.26, and a sketch of the double dipole cell in Fig. 8.27. Table 8.2 details the parameters of the synchrotron resorted to in these simulations.

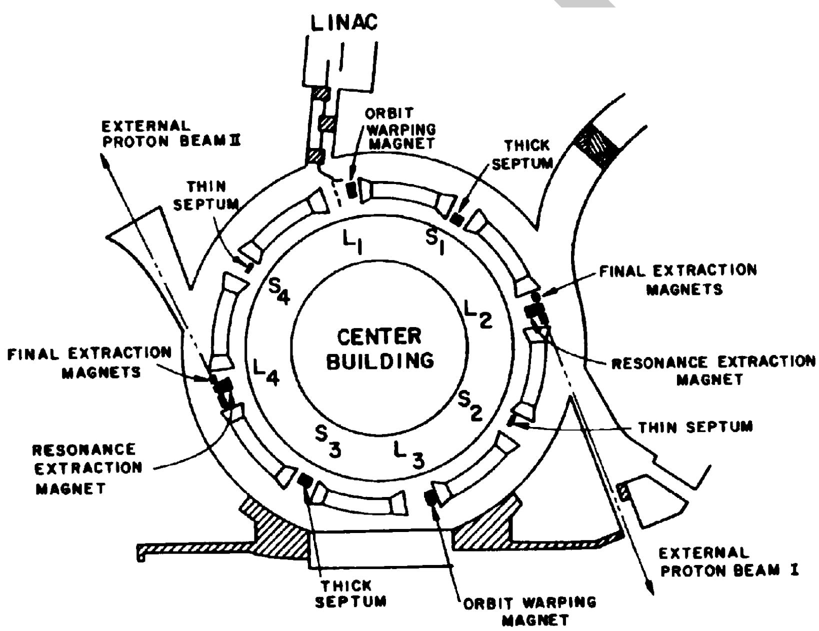

Fig. 8.26 A schematic layout of the ZGS [33], a $\pi/2$-periodic structure, comprised of 8 zero-index dipoles, 4 long and 4 short straight sections

(a) Construct a model of ZGS 45^o cell dipole in the hard-edge model, using DIPOLE. Use the parameters given in Tab. 8.2, and Figs. 8.26, 8.27 as a guidance.

For beam monitoring purposes, split the dipole in two 22.5^odeg halves. Take the closed orbit radius as the reference RM=2076 cm in DIPOLE: it will be assumed that the orbit is the same at all energies[7]. Take an integration step size in centimeter range - small enough to ensure numerical convergence, as large as doable for fast multiturn raytracing.

Validate the model by producing the 6×6 transport matrices of both dipole (MATRIX[IFOC=0] can be used for that, with OBJET[KOBJ=5] to define a proper set of paraxial initial coordinates) and checking against theory (Sect. 14.1, Eq. 14.7).

Add fringe fields in DIPOLE[λ,$C_0 - C_5$], the rest if the exercise will use that model. Take fringe field extent and coefficient values

$$\lambda = 60\,\mathrm{cm}\; C_0 = 0.1455,\; C_1 = 2.2670,\; C_2 = -0.6395,\; C_3 = 1.1558,\; C_4 = C_5 = 0 \tag{8.55}$$

($C_0 - C_5$ determine the shape of the field fall-off, they have been computed from a typical measured field profile $B(s)$).

(b) Construct a model of ZGS cell accounting for dipole fringe fields, with origin at the center of the long drift. In doing so, use DIPOLE[KPOS] to cancel the closed orbit coordinates at DIPOLE ends.

Compute the periodic optical functions at cell ends, and cell tunes, using MATRIX[IORD=1,IFOC=11] (or OBJET[KOBJ=6] and MATRIX[IORD=2,IFOC=11]); check their values against theory.

Move the origin at the location (azimuth s along the cell) of the betatron functions extrema: verify that, while the transport matrix depends on the origin, its trace does not. Verify that the local betatron function extrema, and the dispersion function, have the expected values.

Produce a graph of the optical functions (betatron functions and dispersion) along the cell.

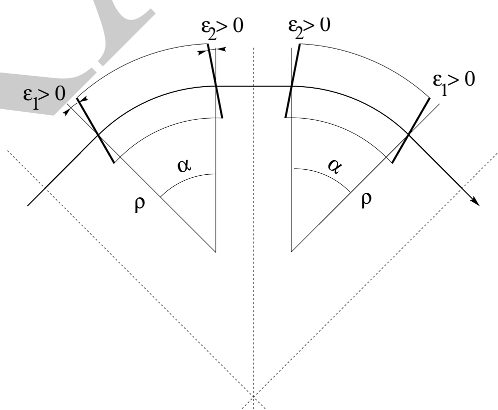

Fig. 8.27 A sketch of ZGS cell layout. In defining the entrance and exit faces (EFBs) of the magnet, beam goes from left to right. Wedge angles at the long straight sections (ε_1) and at the short straight sections (ε_2) are different

(c) Additional verifications regarding the model.

[7] Note that in reality the reference orbit in ZGS moved outward during acceleration [37].

DRAFT

Table 8.2 Parameters of the ZGS weak focusing synchrotron after Refs. [37, 38] [33, pp. 288-294,p. 716] (2nd column, when they are known) and in the present simplified model and numerical simulations (3rd column). Note that the actual orbit moves during ZGS acceleration cycle, tunes change as well - this is not taken into account in the present modeling, for simplicity

		From Refs. [37, 38]	**Simplified model**
Injection energy	MeV	50	
Top energy	GeV	12.5	
$G\gamma$ span		1.888387 - 25.67781	
Length of central orbit	m	171.8	170.90457
Length of straight sections, total	m	41.45	40.44
Lattice			
Wave numbers ν_x; ν_y		0.82; 0.79	0.849; 0.771
Max. β_x; β_y	m		32.5; 37.1
Magnet			
Length	m	16.3	16.30486 (magnetic)
Magnetic radius	m	21.716	20.76
Field min.; max.	kG	0.482; 21.5	0.4986; 21.54
Field index		0	
Yoke angular extent	deg	43.02590	45
Wedge angle	deg	≈10	13 and 8
RF			
Rev. frequency	MHz	0.55 - 1.75	0.551 - 1.751
RF harmonic h=$\omega_{\rm rf}/\omega_{\rm rev}$		8	
Peak voltage	kV	20	200
B-dot, nominal/max.	T/s	2.15/2.6	
Energy gain, nominal/max.	keV/turn	8.3/10	100
Synchronous phase, nominal	deg	150	
Beam			
ε_x; ε_y (at injection)	$\pi\mu$m	25; 150	
Momentum spread, rms		3×10^{-4}	
Polarization at injection	%	>75	100

Produce a graph of the field B(s)

- along the on-momentum closed orbit, and along off-momentum chromatic closed orbits, across a cell;

- along orbits at large horizontal excursion;

- along orbits at large vertical excursion.

For all these cases, verify qualitatively, from the graphs, that $B(s)$ appears as expected.

(d) Justify considering the betatron oscillation as sinusoidal, namely,

$$y(\theta) = A\, \cos(\nu_y\theta + \phi)$$

wherein $\theta = s/R$, $R = \oint ds/2\pi$.

(e) Produce an acceleration cycle from 50 MeV to 17 GeV about, for a few particles launched on a common $10^{-5}\,\pi$m vertical initial invariant, with small horizontal invariant. Ignore synchrotron motion (CAVITE[IOPT=3] can be used in that case).

DRAFT

Take a peak voltage $\hat{V} = 200\,\mathrm{kV}$ (this is unrealistic but yields 10 times faster computing than the actual $\hat{V} = 20\,\mathrm{kV}$, Tab. 8.2) and synchronous phase $\phi_s = 150\,\mathrm{deg}$ (justify $\phi_s > \pi/2$). Add spin, using SPNTRK, in view of the next question, (f).

Check the accuracy of the betatron damping over the acceleration range, compared to theory. How close to symplectic the numerical integration is (it is by definition *not* symplectic [29, Eq. 1.2.4]), depends on the integration step size, and on the size of the flying mesh in the DIPOLE method [36, Fig. 20]; check a possible departure of the betatron damping from theory as a function of these parameters.

Produce a graph of the evolution of the horizontal and vertical wave numbers during the acceleration cycle.

(f) Using the raytracing material developed in (e): produce a graph of the vertical spin component of a few particles, and the average value over the 200 particle bunch, as a function of $G\gamma$. Indicate on that graph the location of the resonant $G\gamma_R$ values.

DRAFT

(g) Based on the simulation file used in (f), simulate the acceleration of a single particle, through one particular intrinsic resonance, from a few thousand turns upstream to a few thousand turns downstream.

Perform this resonance crossing for different values of the particle invariant. Determine the dependence of final/initial vertical spin component value, on the invariant value; check against theory.

Re-do this crossing simulation for a different crossing speed. Check the crossing speed dependence of final/initial vertical spin component so obtained, against theory.

(h) Introduce a vertical orbit defect in the ZGS ring.

Find the closed orbit.

Accelerate a particle launched on that closed orbit, from 50 MeV to 17 GeV about, produce a graph of the vertical spin component.

Select one particular resonance, reproduce the two methods of (g) to check the location of the resonance at $G\gamma_R$ =integer, and to find its strength.

8.3 Visible SR from GEC 70 MeV Synchrotron

Solution: page **??**.

Produce the electric field impulse radiated by a 70 MeV electron in GEC synchrotron, as observed at a vertical elevation $\psi \neq 0$ in a plane tangent to the orbit. MULTIPOL can be used to simulate a trajectory arc of a few $1/\gamma$ deviation. Set IL=2 to log stepwise particle coordinates in zgoubi.plt.

Produce the spectral brightness of the radiation ai that direction.

`Zpop` menu 8/16 can be used for these two questions. An alternative is to program the equations of concern (Eq. 8.36 et seqs.) in an interface, in python for instance.

The 70 MeV orbit radius in GEC synchrotron is 29.2 cm.

References

1. Veksler, V. I.: A new method of accelerating relativistic particles, Comptes-Rendus de l'Académie des Sciences de l'URSS, 43, 8 (1944), p. 329-331
2. McMillan, E. M.: The Synchrotron. Phys. Rev. 68 143-144 (1945)
3. Goward, F. K., and Barnes, D. E.: Experimental 8 MeV synchrotron for electron acceleration. Nature 158, 413 (1946)
4. Pollock, H.C.: The discovery of synchrotron radiation. American Journal of Physics, 1983
5. Elder, F. R., et al.: Radiation from Electrons in a Synchrotron. Phys. Rev. 71, 829 - Published 1 June 1947
6. Kerst, D. W.: The Acceleration of Electrons by Magnetic Induction.. Phys. Rev., 60, 47-53 (1941)
7. SATURNE 1 photos: credit CEA Saclay. Archives historiques du CEA. Copyright CEA/Service de documentation
8. Sessler, A., Wilson, E.: Engines of Discovery. A Century of Particle Accelerators. World Scientific, 2007
9. Fig. 8.3: Credit Reider Hahn, Fermilab
10. Endo, K., et al.: Compact proton and carbon ion synchrotrons for radiation therapy. MOPRI087, Proceedings of EPAC 2002, Paris, France; pp. 2733-2735. https://accelconf.web.cern.ch/e02/PAPERS/MOPRI087.pdf

DRAFT

11. Vostrikov, V.A., et al.: Novel approach to design of the compact proton synchrotron magnetic lattice. tupsa17, 26th Russian Particle Accelerator Conference RUPAC2018, Protvino, Russia (2018).
https://accelconf.web.cern.ch/rupac2018/papers/tupsa17.pdf
12. Symon, K.R.: MURA Days. Proceedings of the 2003 Particle Accelerator Conference.
https://accelconf.web.cern.ch/p03/PAPERS/WOPA003.PDF
13. Ohkawa, T.: Two-beam fixed field alternating gradient accelerator. Rev. sci. Instrum., 29, p. 108-17, 1
14. Bernardini, Carlo: AdA: The First Electron-Positron Collider. Phys. perspect. 6 (2004) 156-183 1422-6944/04/020156-28 DOI 10.1007/s00016-003-0
15. Image by Argonne National Laboratory, comm. L.A. Martinez, ANL, April 2023
16. Cohen, D, : Feasibility of Accelerating Polarized Protons with the Argonne ZGS. Review of Scientific Instruments 33, 161 (1962).// https://doi.org/10.1063/1.1746524
17. Ratner, L.G. and Khoe, T.K.: Acceleration of Polarized Protons in the Zero Gradient Synchrotron. Procs. PAC 1973 Conference, Washington (1973).
http://accelconf.web.cern.ch/p73/PDF/PAC1973_0217.PDF
18. Bywatwr, J., Khoe, T., et al.: A pulsed quadrupole system for preventing depolarization. IEEE Transactions on Nuclear Science (Volume: 20, Issue: 3, June 1973)
19. Cho, Y., et als.: Effects of depolarizing resonances on a circulating beam of polarized protons during or storage in a synchrotron. IEEE Trans. Nuclear Science, Vol.NS-24, No.3, June 1977
20. Parker, E.F.: High Energy Polarized Deuterons at the Argonne National Laboratory Zero Gradient Synchrotron. IEEE Transactions on Nuclear Science, Vol. NS-26, No. 3, June 1979, pp 3200-3202
21. Suddeth, D.E., et als.: Pole face winding equipment for eddy current correction at the Zero Gradient Synchrotron. Procs. PAC 1973 Conference, Washington (1973).
http://accelconf.web.cern.ch/p73/PDF/PAC1973_0397.PDF
22. Rauchas, A.V. and Wright, A.J.: Betatron tune profile control in the Zero Gradient Synchrotron (ZGS) using the main magnet pole face windings. Procs. PAC1977 conference, IEEE Trans. on Nucl. Science, VoL.NS-24, No.3, June 1977
23. Floquet, G.: Sur les équations différentielles linéaires à coefficients périodiques. Annales scientifiques de l'E.N.S. 2e série, tome 12 (1883), p. 47-88.
http://www.numdam.org/item?id=ASENS_1883_2_12__47_0
24. Leleux, G.: Accélérateurs Circulaires. Lecture Notes, INSTN, CEA Saclay (1978)
25. T. Risselada: Transition Gamma Jump Schemes. Proceedings of Jyv askyl a CERN Accelerator School, 7-18 Sept. 1992. Yellow Report CERN 94-01
26. Hofmann, A.: The Physics of Synchrotron Radiation. Cambridge Monographs on Particle Physics, Nuclear Physics and Cosmology (20), Cambridge University Press (2004).
27. Méot, F.: A theory of low frequency far-field synchrotron radiation Particle Accelerators, Vol. 62, pp 215-239 (1999) components as seen by
28. . Méot, F., Ponce, L., Ponthieu, N.: Low frequency interference between short SR sources. PRST-AB, Vol. 4, 062801 (2001)
29. Méot, F.: Zgoubi Users' Guide. https://www.osti.gov/biblio/1062013-zgoubi-users-guide.
Sourceforge latest version: https://sourceforge.net/p/zgoubi/code/HEAD/tree/trunk/guide/Zgoubi.pdf.
30. Leleux, G.: Traversée des résonances de dépolarisation. Rapport Interne LNS/GT-91-15, SATURNE, Groupe Théorie, CEA Saclay (février 1991)
31. Méot, F.: Spin Dynamics. In: Polarized Beam Dynamics and Instrumentation in Particle Accelerators, USPAS Summer 2021 Spin Class Lectures, Springer Nature, Open Acess (2023).
https://link.springer.com/book/10.1007/978-3-031-16715-7
32. Lee, S.Y.: Spin Dynamics and Snakes in Synchrotrons. World Scientific, 1997
33. Khoe, T.K., et al.: The High Energy Polarized Beam at the ZGS. Procs. IXth Int. Conf on High Energy Accelerators, Dubna, pp. 288-294 (1974).
Fig. 8.19: Copyrights under license CC-BY-3.0, https://creativecommons.org/licenses/by/3.0; no change to the material
34. Froissart, M. and Stora, R.: Dépolarisation d'un faisceau de protons polarisés dans un synchrotron. Nucl. lnst. Meth. 7 (l960) 297.

DRAFT

35. Bruck H., Debraine P., Levy-Mandel R., Lutz J., Podliasky I., Prevot F., Taieb J., Winter S.D., Maillet R., Caractéristiques principales du Synchrotron à Protons de Saclay et résultats obtenus lors de la mise en route, rapport CEA no.93, CEN-Saclay, 1958.
36. Méot, F.: Zgoubi Users' Guide.
https://www.osti.gov/biblio/1062013-zgoubi-users-guide Sourceforge latest version:
https://sourceforge.net/p/zgoubi/code/HEAD/tree/trunk/guide/Zgoubi.pdf
37. Foss, M.H., et al.: The Argonne ZGS Magnet. IEEE 1965, pp. 377-382, June 1965
38. Klaisner, L.A., et al.: IEEE 1965, pp. 133-137, June 1965
39. A post-processing tool to transport betatron functions step-by-step, using raytracing data stored in zgoubi.plt.
https://sourceforge.net/p/zgoubi/code/HEAD/tree/trunk/toolbox/betaFromPlt/
40. Aniel, T., et al.: Polarized particles at SATURNE. Journal de Physique, Colloque C2, supplément au n02, Tome 46, février 1985, page C2-499.
https://hal.archives-ouvertes.fr/jpa-00224582
41. The Fortran tunesFrmFai_iterate.f, together with a README and an example of its use, can be found at
https://sourceforge.net/p/zgoubi/code/HEAD/tree/trunk/toolbox/tunesFromFai/
42. https://stackoverflow.com/questions/42677017/plot-average-of-nth-rows-in-gnuplot
43. Méot, F.: Spinor Methods. In: Polarized Beam Dynamics and Instrumentation in Particle Accelerators, USPAS Summer 2021 Spin Class Lectures, Springer Nature, Open Access (2023).
https://link.springer.com/book/10.1007/978-3-031-16715-7

DRAFT